A

ACOUSTIC RADIATION

Alain Weill
Bur. Jussieu, LATMOS, Laboratoire Atmosphere Milieux Observations Spatiales, Paris, France

Definition

Acoustic. One branch of physics which studies sound.

The word acoustic comes from the Greek word *akoustikos*. "which is related to hearing."

Sound. It comes from the Latin word *sonum*: "which is related to the hearing sensation created by perturbation of the material medium (elastic, fluid, solid)." In physics, it is a vibration, generally in a gas, created by expansion and compression of gas molecules. Sound waves propagate in the fluid medium and do not propagate in the vacuum. Sounds can be produced in the atmosphere and oceans by living animals or by structures through interaction with the wind, as, for example, trees murmuring, mountains roaring, river sounds, and waves breaking and can be created by various instruments such as music instruments, microphones, speakers, and transducers and also by instruments developed for remote sensing such as SONAR (Sound Navigation and Ranging), ADCP (Acoustic Doppler Current Profiler), and SODAR (Sound Detection and Ranging or what are called echo sounders for atmosphere and ocean). A sound propagating in a medium is characterized by its speed c:

$$c^2 = \partial P / \partial \rho \tag{1}$$

where P is the pressure and ρ the density, and ∂ is derived.

In a gas,

$$c = (\gamma P/\rho)^{1/2} \tag{2}$$

where γ is the heat capacity ratio.

Notice that sound speed in the air for standard conditions of temperature and pressure near the surface is close to 340 m/s, while at the ocean surface it is close to 1,500 m/s, which is faster. This will have an incidence on different ways for acoustic signal processing to be done in the ocean and atmosphere.

Sound or rather a sound wave is a mechanical pressure oscillation, which is generally longitudinally propagating.

Period T. It is the signal duration corresponding to the time when the sound wave is reproduced identically.

Frequency. $f = 1/T$ (T in s and f in hertz). *Frequency audio spectrum* (distribution of acoustic energy as function of frequencies can be divided in four zones related to human hearing power: 0–20 Hz infrasound (not audible), 20–300 Hz is low-pitched, 300–6,000 Hz is medium range, 6,000–20,000 Hz is high-pitched, more than 20,000 Hz are ultrasonic sounds (not audible).

Sound amplitude. It corresponds to acoustic pressure fluctuation of the medium Δp (amount of energy in the sound wave) measured at one point of a surface S. It is the ratio of pressure P by the surface element S.

$I = P/S$ in W/m^2

For a spherical acoustic source, the intensity at distance r is

$$Ir = P\,(\text{sound power of the source})/4\pi r^2$$

Radiation. It is the way acoustic wave energy radiates and concerns acoustic rays from the acoustic sources through

E.G. Njoku (ed.), *Encyclopedia of Remote Sensing*, DOI 10.1007/978-0-387-36699-9,

the concerned medium. For example, from a microphone radiating along different directions, we are interested in the radiation diagram corresponding to the knowledge of *rays* (analogy with optical rays) along different directions.

Introduction

We shall begin to analyze (sound) or (acoustic) waves and the wave equation from which we are able to describe energy propagation and rays. If one compares them to electromagnetic waves, acoustic waves are simpler and can be described by the velocity potential, which is a scalar. We shall apply the principles of acoustic wave radiation to different types of acoustic sources used such as monopolar, dipolar sources and the response of the medium at different distances showing that the acoustic field will change of as the characteristics do so. These considerations are really fundamental for remote sensing with acoustic sounders and they are similar to electromagnetic waves, though propagation equations are different. They give information about distances when field characteristics will present some useful organization properties.

Wave equation and acoustic waves in flows

It corresponds to the study of a *plane wave* transmitted in a flow by a vibrating plane. It can be, for example, the diaphragm of a microphone vibrating along an axis x.

A *plane acoustic wave* is a general concept from the physics of waves. It corresponds to a wave where *wave fronts* (surfaces of the same phase) are infinite planes, perpendicular to the same direction of propagation.

The equation of pressure variation p (or wave propagation equation) is

$$\partial^2 p/\partial x^2 = \left[1/c^2\right] \partial^2 p/\partial t^2 \tag{3}$$

where, as already said, c is the sound speed.

For a sinusoidal wave, the solution of the equation is

$$p(x,t) = p_0 \cos[(2\pi/T)(t - x/c)] \tag{4}$$

with the wave number $k = 2\pi/T_c = 2\pi/\lambda$ and λ is the wave length.

We get

$$p(x,t) = p_0 \cos(2\pi\, t/T - kx) \tag{5}$$

where $2\pi/T$ is the *pulsation* ω.

Generally, one uses the complex notation:

$$p(x,t) = p_0 \exp(\omega t - kx) \tag{6}$$

A linear relation between the displacement gradient (compressibility) gives $p = -\kappa\ \partial\zeta/\partial x$ (where κ is a coefficient of compressibility) from which we have, solving the sound equation:

$$\partial\zeta/\partial t = (1/(\rho_0 c) \exp(\, j(\omega t - kx)) \tag{7}$$

This means that particle velocity is in phase with acoustic pressure.

Other derived definitions are useful parameters for remote sensing techniques as the acoustic impedance Z, which is the ratio between pressure and the complex amplitude of the particle.

To illustrate the interest in using acoustic impedance, in a project for the Titan satellite sounding (Weill and Blanc, 1987), it was suggested to use acoustic impedance from the satellite's surface to discriminate, by acoustic remote sensing, between solid and liquid surface just before a possible crash of the rocket at the satellite's surface.

For the flow, it is equal to $Zc = \rho_0 c$.

For the plane wave (or *progressive* wave) $\forall\, x$, we have $Z(x) = Zc$.

The *condensation* of the wave is the spatial derivative $-\partial\zeta/\partial x$, which corresponds to a relative change of density.

Monopoles, dipoles, and pulsing sphere

If wave propagation Eq. 3 is satisfied, we can work with harmonic solutions of the equation and use wave superposition in the Fourier space. Let us consider one source S of strength q radiating at radial distance r and the solution of the equation for particles radial velocities is

$$v = \mathrm{A}\left(\exp\left(-jkr\right)/r^2 + jk\, \exp\left(-jkr\right)\right)/r \tag{8}$$

A is a constant and the boundary conditions are such that the solution vanishes at infinity. It is important to notice that radiation behavior is different as function of distance.

The acoustic flux Fa of the radial velocity v across a sphere of radius is id v*$4\pi r^2$ (sphere considered at the distance r) is

$$Fa = 4\pi \mathrm{A}\left(\exp(-jkr) + jkr\, \exp(-jkr)\right) \tag{9}$$

Therefore, when kr is small, the first term of (Eq. 9) predominates and the conditions correspond to what is called the *near field* (velocity in phase with the source), and when kr is large, we are in the *far field* conditions (velocity 90° in advance with the source). These very simple statements are very important in acoustic remote sensing, if (for example) active sea foam, which is an acoustic transmitter at the sea surface, has to be modeled; see Vagle and Farmer (1992) to understand acoustic noise below the surface and bubble sound emission.

A more general representation of acoustic sources corresponds to dipolar sources constituting two radiating sources of strengths or magnitudes $q+$ and $q-$ separated by a distance a and such that $m = qa$ is the *dipolar momentum* (as considered in electromagnetism).

Solving the wave equation for the two monopoles with θ the angle between r and the direction of the dipole gives two velocity components: (a) one for the near field (small r): $m(1 + jkr)\ \exp(-jkr)\ \cos(\theta)/4\pi r^3$, to which is added a transverse component varying as sin θ (orthogonal component), and (b) one for the far field (large r): $-k^2 m\ \cos(\theta)\exp(-jkr)/4\pi r$, which is typically a radial component. Dipolar sources or a combination of dipolar sources are very useful to simulate acoustic antennas and

Acoustic Radiation, Figure 1 Realization of a three offset antennas for a 6 kHz minisounder. One antenna is *vertical* and two others are *slanting*. One distinguishes compression chambers as acoustic sources and the horns and antennas parts (*parabolic* portion + *circular* aperture covered by acoustic foam).

acoustic sources. Moreover, field analysis considering the distance where the field can be considered as far is very important to interpret, for example, signals coming from *active systems* (which transmit acoustic waves) or *passive systems* (which only receive acoustic waves as *acoustic radiometers* by analogy with electromagnetic and optical radiometers.

Close to monopoles and dipoles, which are theoretical concepts, is the pulsating sphere of radius a. With the condition that $ka << 1$, it is shown (for low displacement velocities) that it is equivalent to the radiation of a dipole source at a sphere's center, with radial velocity at the surface equal to $m \cos(\theta)\, 2\pi a^3$ with $m = 2\pi a^3 U_0$, where U_0 is the amplitude of the velocity. This analogy between dipoles and pulsing spheres is very useful to solve a large amount of questions relative to acoustic environment such as bubble acoustic emission.

A main question in the domain of acoustic radiation and for remote sensing purposes using transmitters and receivers corresponds to antenna design. Acoustic radiation does not concern very thin beams as in the optical domain but rather larger beams, and it is necessary to know precisely beam angles to determine the observation volumes. Once the acoustic source has been chosen as *microphones*, *loudspeakers*, *transducers*, *or compression chambers*, which convert electricity in pressure fluctuations and acoustic waves, we next choose an antenna to transmit and receive acoustic waves through the considered medium.

Different types of antennas are used (as multi-beam antennas, synthetic antennas combining different elementary sources, horn and parabolic antennas), from which several properties of transmitted and received signals must be reached: *directivity*, which corresponds to being able to get a signal in a preferential direction, *antenna beam control*, which concerns the knowledge and design of antenna beam angle and to limit secondary beams to a very low level, as, for example, for atmospheric sounding with SODAR.

For the first acoustic sounders, parabolic antennas have been mainly used; see Neff and Coulter (1986). Though it is easy to theoretically and analytically model such antennas, it often needs heavy computation; see Rocard (1951). A validation of antenna design in an *anechoic chamber* (a shielded room designed to attenuate wave echoes caused by reflections from the internal surfaces of the room), at least to test far-field behavior, is always necessary to qualify the antenna response. This makes necessary the use of large anechoic chambers to realize far-field conditions. Whatever is the antenna design, a perfect knowledge of antenna beam is necessary and will limit unpleasant surprises as important secondary beams or a beam larger than what was wanted could occur.

In Figure 1, we show experimental results obtained from the design of an *offset antenna* for a 6 kHz acoustic sounder controlled in an anechoic chamber. An offset dish antenna is a type of satellite dish. It is so-called offset because the antenna feed is offset to the side of the

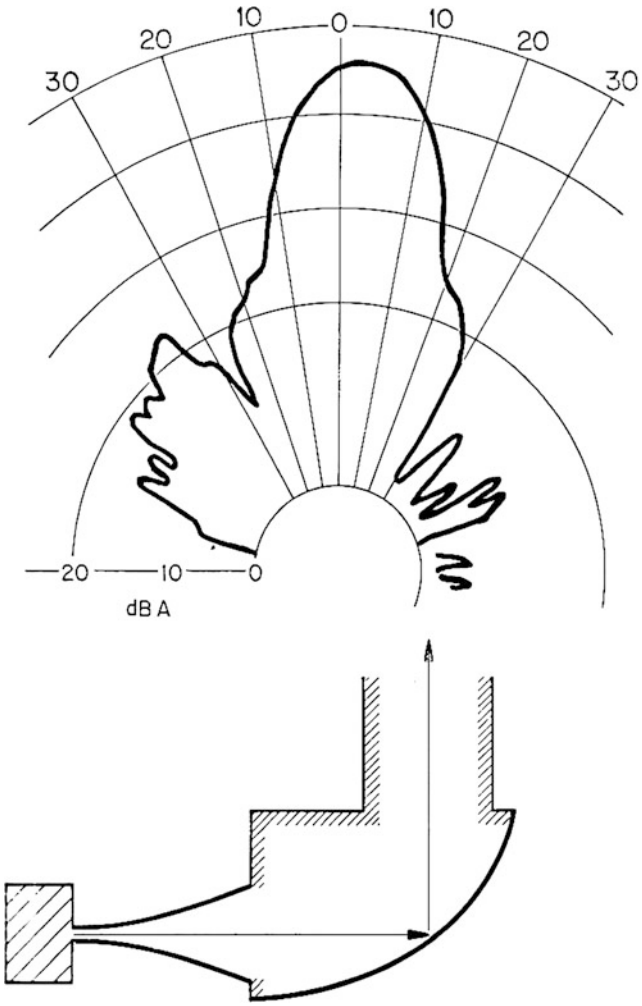

Acoustic Radiation, Figure 2 At the *top*, antenna beam characteristics as measured in an anechoic chamber. At the *bottom*, a simple schema of the antenna characteristics showing an exponential horn transmitting sound in a portion of *parabola*.

reflector, in contrast to a typical circular parabolic antenna where the feed is in front of the center of the reflector.

The antenna's characteristics are shown on Figure 2. Notice that if directivity is good and if secondary beams are relatively low, the antenna beam always differs from theory since it is not easy to model all the elements of the antenna and anyway we have always to validate the modeling. However, a beam width of 13° and a receiver gain of 116–126 dB were obtained, which were in fact the objectives of the design.

Conclusion

We have presented elementary elements about acoustic radiation. Of course, acoustic radiation study in the atmosphere and ocean requires deep specific studies, but considering acoustic remote sensing, questions must be mainly summed up to in regard to radiation pattern of acoustic sources and to antenna design. However, monopole and dipole behavior and also more complicated concepts such as quadripoles and higher acoustic poles systems, which are not presented here, suggest what kind of questions have generally to be solved.

Bibliography

http://mysite.du.edu/~jcalvert/waves/radiate.htm

Neff, W. D., and Coulter, R., 1986. Acoustic remote sensing. In Lenschow, D. (ed.), *Probing the Atmospheric Boundary Layer*. Boston, MA: American Meteorological Society, Vol. 201, p. 242.

Rocard, Y., 1951. *Dynamique générale des vibrations*, 4th edn. Paris: Masson & Cie, 459 pp.

Vagle, S., and Farmer, D. M., 1992. The measurement of bubble size distributions by acoustical backscatter. *Journal of Atmospheric and Oceanic Technology*, **49**(9), 630–644.

Weill, A., and Blanc, M., 1987. Design of an acoustic package for Titan boundary layer and surface properties knowledge: the ASTEK system (Acoustic System for Titan Environment Knowledge). In *Proceedings of the 'CASSINI Surface Workshop'*. Washington, DC: E.S.A., 16 pp.

Cross-references

Acoustic Waves, Propagation
Acoustic Waves, Scattering

ACOUSTIC TOMOGRAPHY, OCEAN

Brian Dushaw
Applied Physics Laboratory, University of Washington, Seattle, WA, USA

Synonyms

Acoustic thermometry; Acoustic Thermometry of Ocean Climate (ATOC); Moving ship tomography; Ocean acoustic tomography (OAT); Reciprocal tomography

Definition

Ocean acoustic tomography is a remote sensing technique that employs the transmission of sound over large distances within the ocean to precisely estimate averages of temperature and current. Acoustic tomography data usually consist of time-of-flight travel times of acoustic pulses, which represent natural integrating measures of sound speed and current along acoustic paths. Variations in sound speed are predominantly caused by variations in temperature.

Introduction

Acoustic tomography is a technique for measuring large-scale ocean temperature and current using acoustic signals propagating over 100–1,000 km distances. The technique relies on the nature of the oceanic sound speed profile, which acts as an acoustic waveguide, and the transparency of the ocean to low-frequency sound. Sound speed is

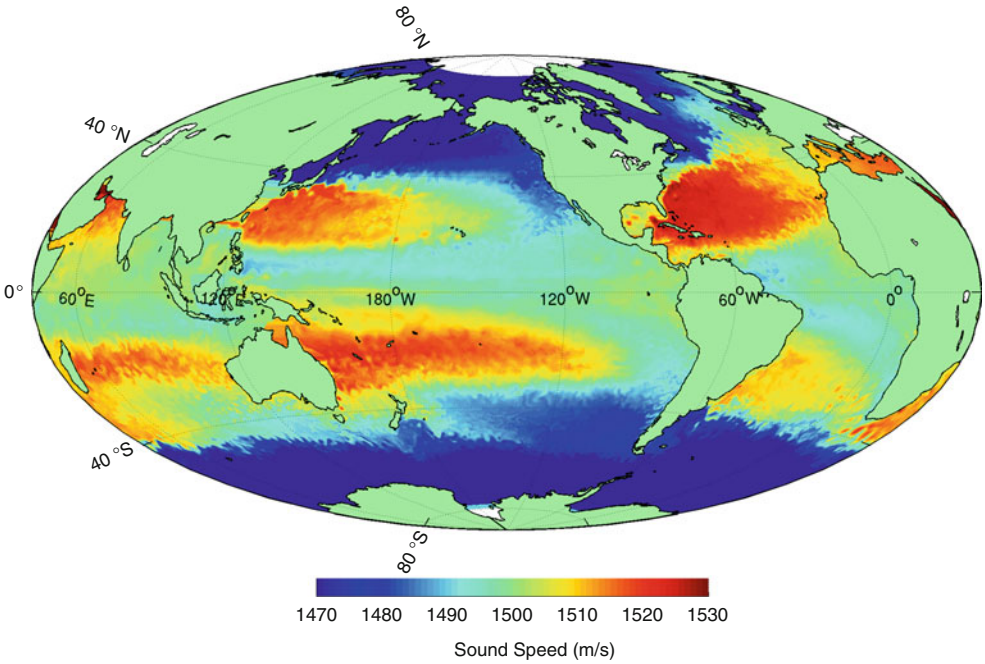

Acoustic Tomography, Ocean, Figure 1 Sound speed at 300 m depth derived from an ocean ocean state estimate from the "Estimating the Circulation and Climate of the Ocean" (ECCO) project. Sound speed is a proxy variable for temperature over most of the world's oceans.

a function of temperature, salinity, and pressure (Jensen et al., 2011), with an approximate value of 1.5 km/s (Figure 1). Over most of the world's oceans, the sound speed profile has a minimum at about 1,000 m depth, with sound speed that increases towards the surface as a result of increasing temperature and increases towards the seafloor as a result of increasing pressure. Acoustic signals are therefore trapped in the sound channel by refraction (Figure 2). By recording time series of travel times of acoustic signals, the variability of ocean temperature can be inferred. A typical acoustic arrival pattern consists of a set of 5–15 pulse arrivals spanning several seconds, corresponding to a set of distinct acoustic ray paths. Tomography is a unique measurement in that it is inherently averaging: over range along the path of acoustic propagation and over depth from the cycling of the acoustic signals over the water column. The measurements of large-scale ocean temperatures and currents can be extraordinarily precise.

The concept of acoustic tomography was originally proposed by Walter Munk and Carl Wunsch in the late 1970s in response to the discovery that mesoscale variability in the ocean was intense and ubiquitous (Munk and Wunsch, 1982; Munk et al., 1995; von Storch and Hasselmann 2010). The mesoscale presented a challenging observational problem for oceanography. The proposed answer to this challenge was the in situ integrating measurements of acoustic tomography combined with the near-synoptic measurements of sea-surface height by satellite altimetry. Several acoustic sources and receivers were to be deployed, forming an array with many acoustic paths crisscrossing a region of interest. The term "tomography" was borrowed from medical tomography, to bring to mind those imaging capabilities. Information available from ocean acoustic tomography is much sparser than from medical tomography, however. From the beginning, the acoustic measurements were to be combined with information from other data types using ocean modeling and data assimilation techniques for optimal estimation of the ocean state (Cornuelle and Worcester, 1996; Menemenlis et al., 1997; The ATOC Consortium, 1998; Rémy et al., 2002; Lebedev et al., 2003).

Sound speed and current

Nominally, a 1 °C change in temperature corresponds to a 4 m/s change in sound speed, while a 1 PSU change in salinity corresponds to a 1.3 m/s change in sound speed. Observed changes in sound speed, measured by tomography through the changes in travel times of acoustic pulses, are therefore ambiguous between temperature and salinity. As a practical matter, however, changes in ocean temperature of 1 °C are common, while changes in ocean salinity of 1 PSU are rare. Other than in extreme environments, the possible effects of salinity changes on acoustic travel times can be ignored.

Ocean currents also affect the time of flight of acoustic pulses, although the magnitudes of current variations are

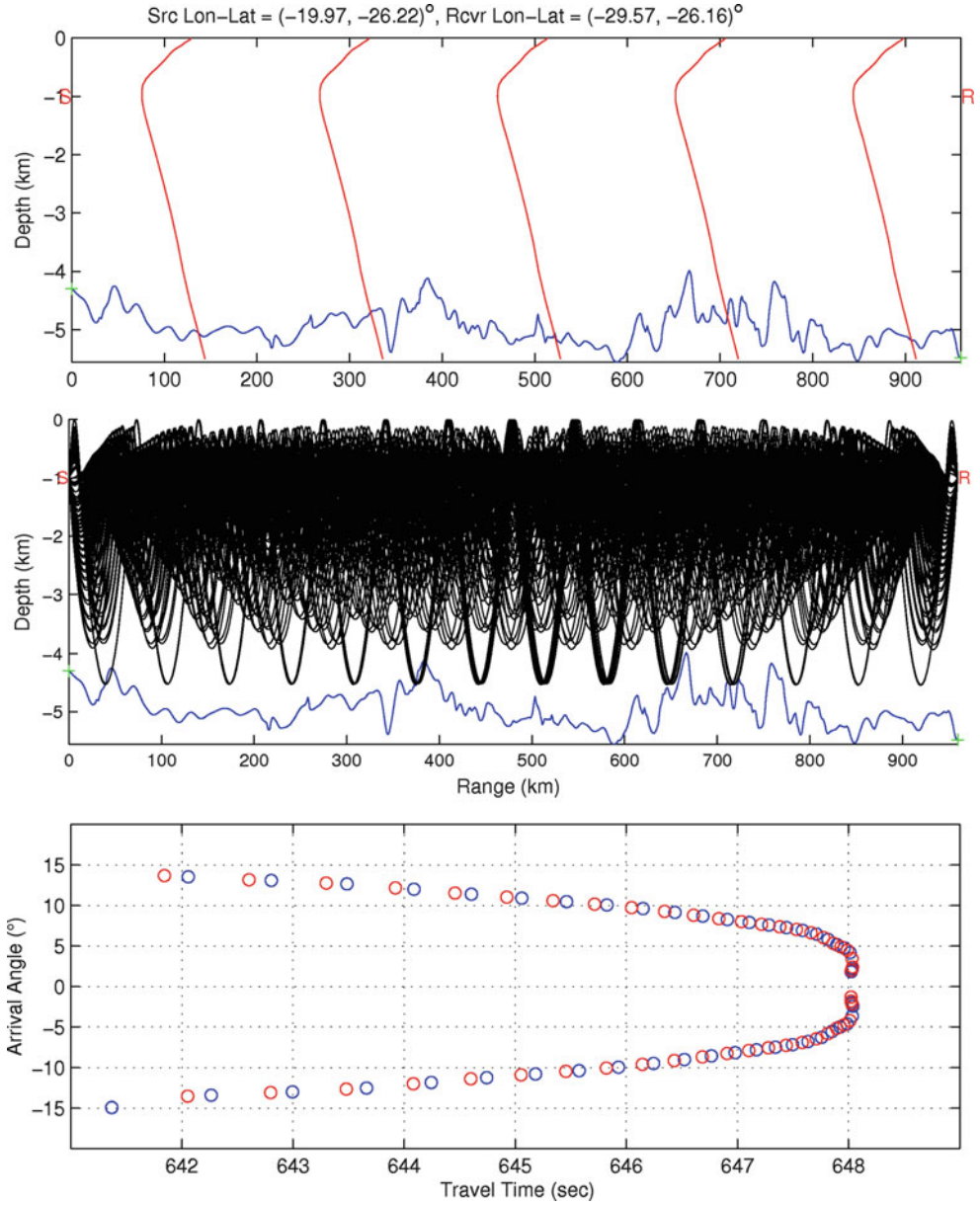

Acoustic Tomography, Ocean, Figure 2 Top: Sound speed profiles derived from the NOAA 2009 World Ocean Atlas along a 960 km section along 26 °S in the Brazil Basin. Middle: Associated acoustic ray paths between a source and a receiver, both at 1,000 m depth. Bottom: Associated ray arrival pattern shown as arrival angle versus travel time. The rays arrive in groups of four, corresponding to the possible signs of the ray angles at the source and receiver. The Brazil Basin has almost ideal characteristics for acoustic tomography. Each region of the ocean has its own unique acoustic properties.

usually an order of magnitude smaller than sound speed variations. The two effects can be separated using reciprocal acoustic transmissions. Reciprocal tomography employs transceivers that transmit coincident signals in opposite directions. The travel times of acoustic pulses with the current will be different than the travel times against the current. By forming the sum and difference of reciprocal travel times, the contributions of sound speed and current can be distinguished.

An early test of reciprocal tomography (RTE87) was conducted in 1987 in the central North Pacific using reciprocal acoustic propagation over ranges of O (1,000 km). Current variations of about 10 mm/s were measured, while sound speed variations were about 25 m/s (Munk et al., 1995). Expressed in terms of acoustic travel times, the nominal time of flight of the acoustic pulses in this experiment was about 600 s, the variations in temperature caused travel time variations of about

0.1 s (summertime warming of the near-surface ocean), and the variations in currents caused travel time variations of about 0.005 s (tidal and low-frequency barotropic currents).

As a corollary to the measurement of current, the integration of currents over the paths of a triangular array of tomographic transceivers is a measure of areal-averaged relative vorticity by Stokes' theorem (Munk et al., 1995). The precision of this measurement can be illustrated by the use of tomography to measure "tidal vorticity" or the changes to relative vorticity primarily induced by the changes in water column depth by tidal elevation. Tidal vorticity of order 10^{-9} s^{-1}, five orders of magnitude less than the planetary vorticity (local inertial frequency), was measured in the western North Atlantic using a pentagonal tomographic array of 660 km diameter deployed in 1991 (Dushaw et al., 1997).

Rays and modes

The determination of information about ocean variability from acoustic data is an inverse problem that requires an ocean model that can be fit to the data using weighted least squares techniques (Munk et al., 1995; Worcester, 2001). Possible models range from a simple time-independent model employing a truncated Fourier series and baroclinic modes to represent horizontal and vertical variability to sophisticated time-dependent dynamical models. The choice of the model depends on the nature of the observed ocean variability and the goals of the oceanographic analysis.

The prerequisite for any inverse problem is a solution for the forward problem, however. Predictions for the acoustic arrival pattern of travel times in any particular experiment geometry can be readily computed by a variety of means, including ray tracing, acoustic modes, or the parabolic wave equation (Jensen et al., 2011). Accounting for a variety of acoustic properties, such as ray travel time and arrival angle, identification of predicted arrivals with measured arrivals is usually unambiguous. This identification is often impossible when the acoustic signals have interacted with the sea floor, however. The tomographic information about the ocean is indicated by the small discrepancies between the predictions and measurements. One goal of this identification is to determine the spatial sampling characteristics, or "measurement kernels," of the acoustics. Most often the measurement kernels are taken to be just the ray paths identified with particular ray arrivals. The measured ray travel times are the integrals of the reciprocal of sound speed along the ray paths. The measurement kernel, combined with the ocean model, enables the essential elements of the inverse problem to be computed, and the weighted least squares solution of that inverse problem gives the desired estimate of ocean variability from the acoustic data.

While acoustic rays have been the measurement kernels most commonly employed for the inversion of tomography data, acoustic modes have also been employed, particularly in polar regions where the polar sound speed profile confines the lowest modes near the surface. The upper ocean is a region of particular interest, of course. The near-surface modes are also sometimes matched to particular water masses in the Arctic (Mikhalevsky and Gavrilov, 2001).

Recently, "travel-time sensitivity kernels" have been computed, which relate the sampling of the complete acoustic wave field to particular travel times (Skarsoulis et al., 2009). Stemming from this rigorous description of the acoustic field was the important proof, long known in practice, that the measurement kernels computed using the geometric-ray approximation are an accurate representation of the actual sampling associated with particular ray arrivals.

Applications

Over the past 30 years, tomography has been employed for wide-ranging applications (Munk et al., 1995; Dushaw et al., 2010). Several examples that highlight the strengths and roles of the measurement will be mentioned here; more substantive reviews of applications can be found in Munk et al. (1995), Dushaw et al. (2001, 2010), and Worcester (2001).

The Greenland Sea Project deployed a six-mooring tomographic array with 100 km diameter in 1988 in the region of deep convective mixing in the Greenland Sea (Morawitz et al., 1996). The Greenland Sea is one of the few regions where deep water of the world's oceans is formed. The aim of the Greenland Sea Project was to quantify this water formation. Tomography was ideal for this measurement because its remote sensing capability was essential in this harsh, sometimes ice-covered, environment, the quantity measured was the net deepwater formation which is an integrated quantity, and the deepwater formation is episodic and unpredictable in time and location. The rapid sampling of integrated temperature afforded by the acoustic measurements proved to be essential in estimating the net deepwater formation over the winter of 1988/1989. Concurrent, extensive measurements by CTD casts proved to be inadequate to the task.

With the ability to make repeated, integrated measurements along an acoustic path, tomography is often employed to monitor temperature or current averaged across straits or other constricted regions. Mass transport and heat content through the Strait of Gibraltar were measured by reciprocal tomography in 1996 (Send et al., 2002). Temperature variations in Fram Strait are presently monitored by tomography by the multiinstitutional ACOBAR collaboration. Within Fram Strait the complicated West Spitsbergen and East Greenland Current systems transport heat and salt between the North Atlantic and Arctic Oceans. One experiment conducted in the late 1990s by the French Research Institute for Exploration of the Sea (IFREMER) aimed to measure the net transport of heat and salt by subsurface

salt lenses, or Meddies, out of the Mediterranean into the North Atlantic.

With its inherent averaging properties, tomography can make unique, accurate measurements of large-scale barotropic currents. The barotropic currents estimated from the RTE87 data had an uncertainty of about 1 mm/s. Relative vorticity associated with the RTE87 currents was of order 10^{-8} s^{-1} (Munk et al., 1995). Measurements of barotropic tidal currents by tomography are the most accurate available; they have been used to test global tidal models. These capabilities have been underutilized in ocean observation.

Whereas the difference of reciprocal travel times is primarily a measure of depth-averaged current, the sum of reciprocal travel times is primarily a measure of the sound speed signature of the first internal or baroclinic mode. The exact resolution of vertical variability, or resolution of higher-order modes, depends on the available vertical sampling of the rays in any particular region. The inherent depth average of the measurement makes the first baroclinic mode the dominant signal, however, when ocean variability is characterized by baroclinic modes. This property led to the detection of radiation of coherent mode-1 internal tides far into the ocean's interior and placed tomography at the forefront of internal-tide and ocean mixing revolution that has unfolded over the past two decades. One interesting aspect of these observations is that an acoustic path acts as line-segment antenna for the internal-tide radiation. The beam pattern for this antenna has narrow maximum response for wave numbers perpendicular to the acoustic path, corresponding to wave crests aligned along the acoustic path. The culmination of these observations, brought together with the more synoptic observations of these waves by satellite altimetry, was the demonstration that mode-1 internal tides propagate coherently across ocean basins. Tidal harmonic constants can be used to predict the amplitude and phase of the mode-1 internal tides over many regions of the world's oceans (Dushaw et al., 2011).

Over the past 30 years, there have been numerous experiments employing multipath tomography arrays for ocean observation. These experiments have taken advantage of the fact that the number of paths of an array increases quadratically with the number of deployed instruments. Experiments have often consisted of a 5 or 6 mooring pentagonal array, as was the case in the Greenland Sea array (Morawitz et al., 1996), the 1990–1991 Acoustic Mid-Ocean Dynamics Experiment (AMODE) in the western North Atlantic (Cornuelle and Worcester, 1996), and the 1997 Kuroshio Extension Pilot Study array (Lebedev et al., 2003). Other experiments have been deployed in the equatorial Pacific (Kaneko et al., 1996). The 2000–2001 Central Equatorial Pacific Tomography Experiment (CEPTE) was aimed at observing the weak meridional currents of the equatorial current system. These experiments have been designed following the original Munk and Wunsch notion to better understand a complicated region by making sparse tomographic observations that are combined with all available ancillary data by ocean modeling and data assimilation techniques. These studies have quantitatively shown that the tomographic data type affords a significant resolution of ocean properties not possible by other data types.

Acoustic thermometry of ocean climate

The use of acoustic transmissions across ocean basins to measure the temperature has come to be called acoustic thermometry. These measurements are made possible by lowering the transmitted acoustic frequency to reduce the sound attenuation. With 20–60 Hz sound signals, the range of acoustic propagation in the ocean does not appear to be limited. The aim of these basin-scale observations is to precisely quantify the large-scale changes in ocean temperature (Dushaw et al., 2001, 2010).

One of the first tests of long-range acoustic transmissions for the purpose of ocean climate measurements was the Heard Island Feasibility Test (HIFT). In a 9 day test in 1991, 57 Hz acoustic signals were transmitted from an array of acoustic sources lowered from the R/V Cory Chouest near Heard Island in the southern Indian Ocean (Munk and Baggeroer, 1994). The site is a location with unblocked acoustic paths to both coasts of the United States, and, indeed, the transmitted signals were recorded off the coasts of Nova Scotia and Washington state. The attempts to measure ocean temperatures over antipodal acoustic ranges were then abandoned with the recognition that measurements across several climatological regimes were perhaps less useful than basin-scale measurements.

The HIFT was succeeded by the decade-long (1995–2006) Acoustic Thermometry of Ocean Climate (ATOC) program (The ATOC Consortium, 1998; Dushaw et al., 2009). This program deployed 75 Hz acoustic sources off central California and north of Hawaii to transmit tomographic signals across the North Pacific Basin. The program employed receivers of opportunity and arrays of hydrophones specifically designed to determine the properties of acoustic propagation over several megameter ranges. The acoustic data were used to test accuracy of ocean state estimates of the North Pacific obtained by various means, including simple forward integration of a model, objective analysis of hydrographic and altimeter data, and assimilation of available data to constrain general circulation models. The travel times measured over a decade were compared with equivalent travel times derived from the several state estimates. The comparisons of computed and measured time series provided a stringent test of the accuracy of the large-scale temperature variability in the models. The differences were sometimes substantial, indicating that acoustic thermometry data does provide significant additional constraints for numerical ocean models.

Averages of temperature across the Arctic Ocean were measured in the 1994 Transarctic Acoustic Propagation (TAP) and 1999 Arctic Climate Observations Using Underwater Sound (ACOUS) experiments (Mikhalevsky

and Gavrilov, 2001). These experiments were among the first observations of warming of the Atlantic Layer in the Arctic Ocean. Using acoustics to remotely sense ocean temperature and other properties under the ice is a particularly compelling application of tomography.

Instrumentation

One of the technical advances that made tomography possible was the development of broadband, controlled sound sources in the 1970s to replace explosive charges. By employing lengthy coded signals and pulse compression techniques, the energy of the sound signals is spread over several minutes, while the travel time resolution achieved after signal processing is about a millisecond. The peak pressure of these controlled signals is much less than signals from the explosive sources. Typical sound levels are 25–250 W (or 185–195 dB re 1 μPa at 1 m). Low-frequency (75–300 Hz), broadband acoustic sources are large and heavy, however. The size of the source is determined by the acoustic wavelength, which, for 250 Hz signals, is 6 m. One acoustic source commonly used today is a tuneable organ-pipe transducer of about 4 m length and 1,000 kg weight that usually broadcasts a swept-frequency signal from 200 to 300 Hz (Figure 3). Broadband acoustic sources, such as the HLF-5, are also power hungry. Moored acoustic sources powered by lithium or alkaline battery packs can transmit coded signals of a few minutes length several times a day for durations of about a year. Timekeeping is maintained using a rubidium atomic clock. The 75 Hz acoustic sources of the ATOC program were mounted on the sea floor and powered and controlled by a cable to shore.

A tomographic receiver typically consists of a small vertical array of about 4 hydrophones spaced by 1.5 wavelengths. Hydrophone arrays allow for beamforming of the received signals, which boosts the SNR of the acoustic arrival pattern and gives a determination of the ray arrival angles. The arrival angle information is important for matching recorded to predicted arrivals and for distinguishing rays that arrive at about the same time but with different angles (Figure 2, bottom). Tomography transceivers usually consist of a mooring with an acoustic source placed near the sound channel axis and a small vertical line array (VLA) immediately above or below. Both instruments are controlled by a single electronics package.

Recently hydrophone modules were developed with the ability to communicate with a controlling electronics package by induction along the mooring wire. These hydrophone modules allow the deployment of VLAs of any number and spacing, since they can be clamped on the mooring wire at arbitrary locations. For acoustics research, VLAs of 100 or more hydrophones have been employed. These modules include thermistors as well, so that a VLA can act as a thermistor chain. Hydrophones have a broadband sensitivity and of course can also be used for studies of ambient sound.

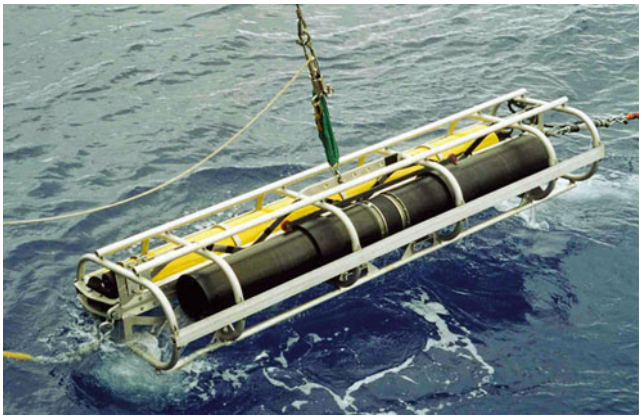

Acoustic Tomography, Ocean, Figure 3 A Webb Research swept-frequency acoustic source as it is deployed from a ship. The black cylinder is the "organ pipe" acoustic source, and the yellow cylinder is an alkaline battery pack. In the photo the source is horizontal; once deployed the right hand side will be oriented towards the surface. The source is mounted within an aluminum cage for protection during shipping and deployment. Courtesy of Lloyd Green, Scripps Institution of Oceanography.

One extension of tomography is the concept of "Moving Ship Tomography." The technique aims to make the most of a deployed array of acoustic sources by circumnavigating this array while repeatedly lowering a hydrophone array from a ship to receive the acoustic signals. The aim is to eventually accumulate enough acoustic data that the temperature field within the circumnavigation can be mapped to considerable resolution. Since it can take up to 60 days to circumnavigate a region of 1,000 km diameter, data assimilation techniques are required to account for the evolution of the temperature field while the data are obtained. Recently hydrophones have been experimentally deployed on gliders to receive signals transmitted by tomographic sources.

Passive tomography is an experimental technique that aims to avoid the expense and trouble of moored acoustic sources by using ambient sounds as tomographic signals. The technique employs coordinated receiving arrays deployed on either side of an area of observation. Ambient sound, preferably from such sources as a distant ship or whale, propagating past one array then forms a known signal when it is received on the second array. By comparing the two acoustic signals, information about the intervening ocean might be inferred.

Marine mammals and active acoustics

The HIFT and ATOC programs engendered considerable controversy concerning the possible effects of the transmitted sounds on marine mammals and other marine life (Potter, 1994). The issue presented a formidable challenge in public relations, since it included marine science, climate, and acoustics topics, many of which are still areas of active research. For example, one newspaper report

confused sound levels in air with those in water, which are defined differently, making the underwater acoustic sources appear to be several orders of magnitude louder than they actually were. The sound transmitted by the ATOC sources was 195 dB re 1 μPa at 1 m (about 250 W), with a low duty cycle (ca. 2 %) consisting of eight brief transmissions every few days. Because of spherical spreading, 1,000 m from the source the signal level was only 135 dB (about 2.5×10^{-4} W).

As a result of the controversy, the 1996–2006 ATOC and NPAL (North Pacific Acoustic Laboratory) projects included a Marine Mammal Research Program (MMRP) to study the potential effects, if any, of the ATOC sound sources on marine mammals and other marine life. (Indeed, the issue of the effects of acoustics on marine mammals proved to be a boon for marine mammal research.) The MMRP did not find any overt or obvious short-term changes in the distribution, abundance, behavior, or vocalizations of marine mammals in response to the playback of ATOC-like sounds or in response to the transmissions of the ATOC sound sources themselves. The MMRP investigators concluded that the ATOC acoustic transmissions caused no significant biological impact (National Research Council, 2000).

Summary

Ocean acoustic tomography uses the travel times of coded acoustic signals transmitted over 100–1,000 km ranges to infer precise information about the ocean temperatures and currents. In most regions of the world's oceans, sound speed is an accurate proxy variable to temperature; salinity contributions are negligible. One primary strength of the measurement is that it is inherently averaging, suppressing the small-scale internal wave or mesoscale noise that can make it difficult to observe the large-scale signal. Predicted acoustic ray paths can be identified with measured multipath arrivals and used in an inverse analysis to estimate ocean variability. Ray paths have been shown to accurately represent the measurement kernel for the recorded arrivals. The variations of both sound speed and current can be estimated using acoustic transmissions sent reciprocally between transceiver pairs.

Tomography data are perhaps best employed by combining them with other data types, such as satellite altimetry and Argo floats, using data assimilation techniques and ocean models. Such techniques bring together dynamical constraints and disparate data types, each with its own sampling, bias, and error characteristics, to obtain optimized state estimates for the ocean.

Over the past 30 years, tomography has been employed for disparate applications, ranging from the quantification of deepwater formation in the Greenland Sea to the detection of internal-tide radiation from the Hawaiian Ridge to basin-wide measurements of temperature in the central North Pacific. Tomography often requires careful analysis and interpretation, depending on the unique acoustic and oceanographic conditions of the region where it is employed. Whether used for regional- or basin-scale observations, acoustic remote sensing has been quantitatively shown to provide information about ocean variability that is not possible to obtain by other approaches.

Acoustic tomography was accepted as part of the emerging Ocean Observing System during both of the OceanObs'99 and '09 international workshops (Dushaw et al., 2001; Dushaw et al., 2010). Within the observing system context, the instrumentation for tomography can serve multiple purposes. Hydrophone arrays are used to study a wide range of human, biological, and geological activity. Acoustic sources can transmit signals that can serve other purposes, such as signals that can be used to track drifting instrumentation. Thus, a modest set of active and passive acoustic instrumentation deployed worldwide can form a general-purpose global acoustic observing network (Howe and Miller, 2004; Boyd et al., 2011).

Bibliography

Boyd, I. L., Frisk, G., et al., 2011. An international quiet ocean experiment. *Oceanography*, **24**, 174–181, doi:10.5670/oceanog.2011.37.

Cornuelle, B. D., and Worcester, P. F., 1996. Ocean acoustic tomography: integral data and ocean models. In Malanotte-Rizzoli, P. (ed.), *Modern Approaches to Data Assimilation in Ocean Modeling*. New York: Elsevier, pp. 97–115.

Dushaw, B. D., Egbert, G. D., Worcester, P. F., Cornuelle, B. D., Howe, B. M., and Metzger, K., 1997. A TOPEX/POSEIDON global tidal model (TPXO.2) and barotropic tidal currents determined from long-range acoustic transmissions. *Progress in Oceanography*, **40**, 337–367.

Dushaw, B. D., et al., 2001. Observing the ocean in the 2000s: a strategy for the role of acoustic tomography in ocean climate observation. In Koblinsky, C. J., and Smith, N. R. (eds.), *Observing the Oceans in the 21st Century*. Melbourne: GODAE Project Office and Bureau of Meteorology, pp. 391–418.

Dushaw, B. D., Worcester, P. F., et al., 2009. A decade of acoustic thermometry in the North Pacific Ocean. *Journal of Geophysical Research*, **114**, C07021, doi:10.1029/2008JC005124.

Dushaw, B. D., et al., 2010. A global ocean acoustic observing network. In Hall, J., Harrison, D. E., and Stammer, D. (eds.), *Proceedings of OceanObs'09: Sustained Ocean Observations and Information for Society*. Venice: ESA Publication WPP-306, Vol. 2.

Dushaw, B. D., Worcester, P. F., and Dzieciuch, M. A., 2011. On the predictability of mode-1 internal tides. *Deep Sea Research*, **58**, 677–698, doi:10.1016/j.dsr.2011.04.002.

Howe, B. M., and Miller, J. H., 2004. Acoustic sensing for ocean research. *Marine Technology Society Journal*, **38**, 144–154.

Jensen, F. B., Kuperman, W. A., Porter, M. B., and Schmidt, H., 2011. *Computational Ocean Acoustics*, Second edn. New York: Springer, doi:10.1007/978-1-4419-8678-8. ISBN 978-1-4419-8677-1.

Kaneko, A., Zheng, H., Nakano, I., Yuan, G., Fujimori, H., and Yoneyama, K., 1996. Long-term acoustic measurement of temperature variations in the Pacific North Equatorial Current. *Journal of Geophysical Research*, **101**, 16,373–16,380, doi:10.1029/96JC01053.

Lebedev, K. V., Yaremchuk, M., Mitsudera, H., Nakano, I., and Yuan, G., 2003. Monitoring the Kuroshio Extension through dynamically constrained synthesis of the acoustic tomography, satellite altimeter and in situ data. *Journal of Oceanography*, **59**, 751–763.

Menemenlis, D., Webb, A. T., Wunsch, C., Send, U., and Hill, C., 1997. Basin-scale ocean circulation from combined altimetric, tomographic and model data. *Nature*, **385**, 618–688.
Mikhalevsky, P. N., and Gavrilov, A. N., 2001. Acoustic thermometry in the Arctic Ocean. *Polar Research*, **20**, 185–192, doi:10.1111/j.1751-8369.2001.tb00055.x.
Morawitz, W. M. L., Sutton, P. J., Cornuelle, B. D., and Worcester, P. F., 1996. Three-dimensional observations of a deep convective chimney in the Greenland Sea during winter 1988/1989. *Journal of Physical Oceanography*, **26**, 2316–2343.
Munk, W., and Baggeroer, A., 1994. The Heard Island papers: a contribution to global acoustics. *Journal of the Acoustical Society of America*, **96**, 2327–2329, doi:10.1121/1.411316.
Munk, W., and Wunsch, C., 1982. Observing the ocean in the 1990s. *Philosophical Transactions of the Royal Society London A*, **307**, 439–464, doi:10.1098/rsta.1982.0120.
Munk, W., Worcester, P., and Wunsch, C., 1995. *Ocean Acoustic Tomography*. Cambridge: Cambridge University Press. ISBN 0-521-47095-1.
National Research Council, 2000. *Marine Mammals and Low-Frequency Sound: Progress Since 1994*. Washington, DC: National Academy Press. 160 pp, http://www.nap.edu/catalog.php?record_id = 9756. ISBN ISBN-10: 0-309-06886-X.
Potter, J. R., 1994. ATOC: sound policy or enviro-vandalism? Aspects of a modern media-fueled policy issue. *The Journal of Environment & Development*, **3**, 47–62, doi:10.1177/107049659400300205.
Rémy, E., Gaillard, F., and Verron, J., 2002. Variational assimilation of ocean tomographic data: twin experiments in a quasi-geostrophic model. *The Quarterly Journal of the Royal Meteorological Society*, **128**, 1739–1458, doi:10.1002/qj.200212858317.
Send, U., Worcester, P., Cornuelle, B. D., Tiemann, C. O., and Baschek, B., 2002. Integral measurements of mass transport and heat content in the strait of Gibraltar from acoustic transmission. *Deep Sea Research Part II*, **49**, 4069–4095, doi:10.1016/S0967-0645(02)00143-1.
Skarsoulis, E. K., Cornuelle, B. D., and Dzieciuch, M. A., 2009. Travel-time sensitivity kernels in long-range propagation. *The Journal of the Acoustical Society of America*, **126**, 2223–2233, doi:10.1121/1.3224835.
The ATOC Consortium, 1998. Ocean climate change: comparison of acoustic tomography, satellite altimetry, and modeling. *Science*, **28**, 1327–1332, doi:10.1126/science.281.5381.1327.
von Storch, H., and Hasselmann, K., 2010. *Seventy Years of Exploration in Oceanography: A Prolonged Weekend Discussion with Walter Munk*. Berlin: Springer-Verlag, doi:10.1007/978-3-642-12087-9. ISBN 978-3-642-12086-2.
Worcester, P. F., 2001. Tomography. In Steele, J., Thorpe, S., and Turekian, K. (eds.), *Encyclopedia of Ocean Sciences*. San Diego: Academic Press, pp. 2969–2986.

Links

Acoustic Technology for Observing the interior of the Arctic Ocean (ACOBAR): http://acobar.nersc.no
The Heard Island Feasibility Test (HIFT): http://909ers.apl.washington.edu/dushaw/heard/
North Pacific Acoustic Laboratory (NPAL): http://npal.ucsd.edu/
Ocean Acoustics Library: http://oalib.hlsresearch.com/
Discovery of Sound in the Sea (DOSITS) http://www.dosits.org/
Ocean acoustic tomography on Wikipedia: http://en.wikipedia.org/wiki/Ocean_acoustic_tomography
A day in the life of a tomography mooring: http://staff.washington.edu/dushaw/mooring/

ACOUSTIC WAVES, PROPAGATION

Alain Weill
Bur. Jussieu, LATMOS, Laboratoire Atmosphere Milieux Observations Spatiales, Paris, France

Synonyms

Acoustic propagation; Sound waves propagation

Definition

Propagation. Concerns acoustical wave transmission inside a solid, liquid, or gaseous physical medium without material entrainment.

Introduction

After a very simple description of acoustical geometric propagation and plane wave assumption at large distance from sources, we shall speak about acoustic absorption by the medium as a function of frequencies and medium parameters. Then we shall present Doppler shift, which is very fundamental for remote sensing techniques. We shall be in a position to discuss sound propagation in a stratified media having some mean properties variation as a function of distance of acoustic sources or receivers. This last question is very important for atmosphere and ocean remote sensing where acoustic ray tracing has to be performed to know how acoustic waves propagate and from what kind of target an acoustic signal comes.

Wave propagation

If a pure sound corresponds to a sinusoidal wave, a sound can generally be considered as a superposition of sinusoidal waves of different frequencies f_i.

At the acoustic source 0, we can say that the sound amplitude is

$$y(0, t) = \sum\nolimits_i (a_i \sin(2\pi f_i t) \quad (1)$$

If the different frequencies at the origin are considered to be in phase, c the wave velocity is supposed not to depend on frequency.

In the entry on "Acoustic Radiation," we have described elementary acoustic sources as monopoles, dipoles, and pulsating spheres. Let us consider an acoustical source at one point, which radiates spherical waves. The acoustic intensity at different distances remains the same, considering all of the sphere points at distance r from the source (repartition in the surface $4\pi r^2$), but the acoustic intensity at each point, at the distance r will be divided by $4\ \pi r^2$. This corresponds to what is called *spherical divergence*. As an easy rule, if the distance is multiplied by 10, the sound intensity will be 100 times smaller.

Notice that far from the source, the wave can be considered as a plane wave.

Wave absorption

Let us consider, as an example, an air layer of depth d and a sound of frequency f_i propagating across this layer. Several observations can be noticed:

If the incident sound has an incident intensity I_{inc}, one part of the sound I_{ref} can be reflected by the layer, one part I_{abs} can be absorbed, and finally one part is transmitted I_{tr}. For the depth d, we can say that the air absorption coefficient corresponds to $a = I_{abs}/I_{inc}$. This absorption coefficient corresponds to absorption at the acoustic frequency f_i.

In the air, sound absorption depends on frequency, temperature, and humidity. A very important reference is Harris (1966), who has performed several laboratory experiments to measure sound attenuation in air (in dB/100 m) as a function of frequency, which is very useful to choose power and frequencies to design acoustic sounders. As the behavior as a function of frequency, of temperature, and humidity is not linear, it is preferable here just to indicate behavior elements and to refer to Harris' (1966) work for precise attenuation evaluation.

It has to be remarked that attenuation grows with frequencies and it presents a maximum, which increases with humidity in percent (maximum of attenuation close to 1 dB/100 m at 2,000 Hz for a typical humidity of 5 % and a maximum of 8.5 dB/100 m for a 20 % of humidity at 25,000 Hz for a temperature of 20 °C).

For humidity between 30 % and 90 %, frequency variation is rather linear (0.3 dB/100 m for 2,000 Hz and 0.8 dB/100 m for 4,000 Hz). Particularly important is to consider that for a chosen frequency, attenuation as function of temperature and humidity in percent presents a maximum, which increases when humidity decreases. Typically, for low humidity below 30 %, attenuation increases as a function of humidity and temperature and for larger temperature (typically higher than 30°), the behavior is reverse and attenuation decreases for higher humidity.

For the ocean, sound absorption is smaller than in the air. It depends on salinity, temperature, and pH (acidity) of the ocean.

Here r is the distance and I_0 is acoustic power transmitted before attenuation. It is close to 0.011 dB/100 m at 2,000 Hz at a 100 m depth. Notice that if the same frequencies as in air are considered for the ocean, wave lengths are, of course, five times larger due to sound speed.

Doppler shift

This very general phenomenon, which is transversal to many remote sensing domains, (electromagnetic, optical, and acoustic), was discovered at the end of the nineteenth century.

For acoustic waves, it corresponds to a frequency shift between a transmitter and a receiver when distances between both change as a function of time. This effect was discovered by an Austrian physicist Christian Doppler in 1842 and confirmed from experiments performed by the Dutch meteorologist Buys Ballot in 1845. Buys Ballot has verified Doppler shift with a special experimental protocol. Musicians were playing horns on a train of known speed and trained musicians on the railway station were hearing sound changes due to train speed.

If f was the transmitted horn frequency played by musicians, f' the frequency observed by fixed musicians in the railway station, c the sound speed, then the Doppler frequency shift due to the train speed can be written as

$$\Delta f/f = (f - f')/f = v/c$$

where v is train speed.

The observed frequency $f' = f + (fv/c)$ is of course dependent on the relative train velocity.

The Doppler shift is very useful for Doppler Sodar or Sonar to be able, using *distance gates* (surface acoustically illuminated at different distances), to analyze medium properties relatively to observed gates. In fact, with these kinds of instruments, mainly the Doppler spectrum is computed to analyze the mean Doppler shift inside different gates. Radial velocities of the medium, in the case where transmitter and receiver are at the same location (for monostatic systems), are measured.

Reflection and refraction of acoustic waves

It corresponds to a general law of propagation of waves corresponding to the Snell-Descartes- Huygens law used for optical waves. However, ocean and atmosphere are *stratified* in temperature, salinity, current for ocean and in temperature, wind, humidity for atmosphere, which corresponds to the fact that we cannot strictly speak of layers since there are more or less continuous variations of these parameters. Let us consider sound reflection in the ocean. In the ocean, the sound velocity mainly depends on the depth z and one supposes that the surface and the bottom of the ocean are (for a first approximation) horizontal planes. One uses generally the concept of ray approximation, and questions which have to be solved correspond to ray tracing. One necessary (but not sufficient condition) to use this concept is that the relative gradient of sound velocity and the wave length must satisfy (see Brekhovskikh and Lysanov, 1990) the condition:

$$\lambda/c(\partial c/\partial z) << 1 \tag{2}$$

We, therefore, apply Snell's law $\cos(\theta)/c(z) = \text{constant}$, where θ is the grazing angle (incidence angle) to vary in thin layers 1,2, . . .n, $n + 1$, where θ_n, θ_{n+1}, c_n, c_{n+1} are, respectively, grazing angles and sound speeds for layers ..n, $n + 1$.

$$\cos(\theta_{n+1})/c_{n+1} = \cos(\theta_n)/c_n \tag{3}$$

and

$$\cos(\theta_{n-1})/c_{n-1} = \cos(\theta_n)/c_n \tag{4}$$

and so on.

When n tends to infinity, then Snell's law is obtained.

With this type of *discretization* (transformation into small layers) of the atmosphere and ocean, one can obtain

propagation in terms of rays and grazing angles tracing. Notice that layers can be obtained considering variations of the main different ocean parameters (salinity, temperature, current) and for the atmosphere (temperature, wind, humidity).

For a considered layer, we get:

$$\theta = [2(c_2 - c_1)/c_1]^{0.5} \quad (5)$$

Therefore, if c_2 is close to c_1, θ is very small.

To determine the relationship between the ray curvature and sound velocity gradient, we can use Snell's law in the form

$c_0 \cos(\theta) = c \cos(\theta_0)$, where c_0 and θ_0 correspond to values at a fixed (height or depth).

Differentiating this equation with respect to z gives

$d\theta/ds = -cos(\theta_0)/c_0 \, dc/dz$ with ds the ray element $= dz/\sin(\theta)$

$\cos(\theta_0)/c_0$ corresponds to the ray path element at a known depth or height.

Abs[$ds/d(\theta)$] is the *curvature* ray R.

To find rays across the atmosphere and the ocean is related to different propagation computer programs, which have been mainly developed for ocean acoustics.

It is important to say a word about sound channel, the SOFAR channel discovered by Ewing and Worzel (1948). At a depth which varies with geographical location at about 1 km of depth, rays tend to bend toward regions of smaller sound speed and are channeled. Refracted rays can extend toward thousands of kilometers in range without touching surface or bottom. This propagation channel works like the ionosphere for electromagnetic propagation and plays a fundamental role for low-frequency acoustic communication; see Munk (2002). It has to be noticed that ocean and/or ocean currents modifications, which can be related to climatic variations, can have an impact on this propagation channel. This justifies acoustic studies of global warming, see Munk and Forbes (1989).

For the atmosphere, stratification related to inversion layers, fronts or stratosphere can play a similar propagation layer for acoustic waves as for ocean, but temporal and spatial variability is larger and we cannot speak of a "permanent channel."

Conclusion

Propagation of acoustic waves in ocean and atmosphere knowledge is mainly dependent on properties of these mediums. Acoustic remote sensing is indeed used to analyze atmosphere and ocean behavior or acoustic targets behavior inside these domains as a Doppler shift related to currents or wind, and/or parameters which influence acoustic propagation. Particularly, acoustic *tomography* (analysis by layers (*tomos* in Greek), which is used to invert ocean or atmosphere properties) needs a perfect knowledge of ray tracing modeling with basic principles of ray tracing similar to those shown in this entry.

Bibliography

Brekhovskikh, L. M., and Lysanov, Y. P., 1990. *Fundamentals of Ocean Acoustics*, 2nd edn. Berlin: Springer, 270 pp.

Ewing, M., and Worzel, J. L., 1948. *Propagation of Sound in the Ocean*. New York: Geological Society of America, Memoir 27.

Flatté, S. M., Dashen, R., Munk, W. M., Watson, K. M., and Zachariasen, F., 1979. *Sound Transmission Through a Fluctuating Ocean*. Cambridge: Cambridge University Press, 299 pp.

Harris, C. M., 1966. Absorption of sound in air versus humidity and temperature. *Journal of Acoustical Society of America*, **40**(1), 148–159.

Munk, W., 2002. Acoustic tomography. In *Encyclopedia of Global Environmental Change*. Chichester: Wiley Editor, Vol. 1, p. 161.

Munk, W. H., and Forbes, A. M. G., 1989. Global ocean warming: an acoustic measure? *Journal of Physical Oceanography*, **19**, 1765–1778.

Cross-references

Acoustic Tomography, Ocean
Electromagnetic Theory and Wave Propagation

ACOUSTIC WAVES, SCATTERING

Alain Weill
Bur. Jussieu, LATMOS, Laboratoire Atmosphere Milieux Observations Spatiales, Paris, France

Definition

Scattering. A way by which obstacles or medium fluctuations of small dimensions can modify acoustic wave propagation in the medium. The difference between scattering processes and the reflection/refraction process is related to acoustic wavelengths. For scattering, acoustic wavelengths are of the order of obstacles and medium fluctuation dimensions. Francisco Maria Grimaldi first described scattering of optical waves in 1665, in the opus *Physicomathesis of lumine*, but this principle was renounced by Fresnel at the end of seventeenth century.

It is important to differentiate between scattering and *diffraction.* Diffraction concerns perturbations whose dimensions are large compared to a wavelength.

Introduction

In the first section, we will describe acoustic scattering by simple obstacles such as spheres. The second section will introduce Lambert scattering and Marsh scattering from surfaces; this process is particularly important for sonar sounding. The third section will introduce acoustic scattering in a turbulent medium; which is useful for understanding propagation in the turbulent atmosphere and ocean. This last process is very fundamental to understanding Sodar (sound detection and ranging) acoustic sounding.

Acoustic scattering of a plane wave on a rigid sphere

Suppose that a plane wave (progressive wave) intercepts a fixed and rigid (not compressible) sphere. As the obstacle is rigid, there is no acoustic emission by the sphere itself and the flow is modified just around the sphere. Here, we use a simple concept of acoustic equivalence to describe acoustic perturbation.

This concept can be summarized as follows.

We examine a small volume (of any shape), and in this case, it is a sphere of shape dimension much less than a wavelength in size. When an acoustic wave intersects the volume, the volume does not transmit any sound since it is not deformed, but it has effects on sound radiation, and sound energy from the incident radiation is scattered in all directions. As in optics, the scattered amplitude is proportional to the wave number at power 4.

1. We have a first perturbation equivalent to a simple acoustic source (monopole) at the center of the sphere that would source and sink sufficient volume to cancel the changes that would occur in its absence.
2. A second perturbation is the same as for a sphere (dipole) oscillating in a medium at rest with a velocity opposite to that of the wave.

Therefore, we can replace the sphere by a single (monopole) and a double source (dipole) located at its center, which has the same effect on the flow at large distances as the sphere did. We assume that $2\pi a/\lambda$ is $\ll 1$, which is equivalent to say that plane wave properties remain constant across the sphere.

This last strict condition on the wavelength and sphere radius has great importance in the choice of wavelengths and frequencies or perturbation dimensions.

The equivalent monopole and dipole will radiate energy in all directions; therefore, the energy in the plane wave will be partially scattered, and we have to evaluate the strength of the equivalent sources.

The change in the incident source is the *condensation* s, which corresponds to the change in volume per unit volume, so the volume compressed into the volume of the sphere is Qs, where Q is the volume of the sphere $4\pi a^3/3$. This would be roughly the same equivalent change for a body of any shape. Hence, the strength of the monopole is the time derivative of this, which gives a strength of $q = -k^2\, Q\, \varphi_0$, q is the strength of the monopole, k the wave number and φ_0 is the source intensity, since the condensation is the derivative of the velocity potential, divided by square of sound velocity in the motion equation. Note that the difference between spatial and temporal derivative is in the factor jk, which makes the difference between temporal and spatial derivative from the wave equation.

The resultant velocity potential from the two equivalent sources acting simultaneously is

$$\varphi = -(ka)^2(2\pi a\varphi_0/3)(2 + 3\,\cos(\theta)) \times (\exp(-jkr)/r) + (ka)(2\pi a\varphi_0)\cos(\theta) \times \exp(-jkr)/r^2) \quad (1)$$

where θ is the angle between r and the direction of the acoustic source. The first term is dominant for large distances, since the second term, corresponding to near field, vanishes rapidly.

Consider now the scattered intensity derived from the acoustic pressure; it is proportional to:

1. The intensity of the incoming source
2. $(ka)^4$
3. The sphere surface cross-section
4. $4 + 12\cos(\theta) + 9\,\cos(\theta)^2$

This is similar as for electromagnetic waves scattering, except for angular dependence.

Integration in all θ shows an equivalent result, as if the dipole and the monopole were independently radiating. (π in radians is equal to 180°)

If A is the amplitude of the displacement, we get a total scattered intensity:

$$W = \left(\pi a^2\right)\left(\rho c\omega^2 A^2/2\right)\ (ka)4\ \ (4/9 + 1/3) \quad (2)$$

where 4/9 comes from the monopole and 1/3 comes from the dipole.

If we divide by the first factor, which is the sphere cross-section, we obtain *the scattering cross-section.*

As for acoustic radiation, monopole and dipole analysis is very useful to simulate scattering if perturbation in the flow can be considered as rigid.

Whatever the different components of the scattered energy are, it is important to notice a strong dependence on wave number at power 4, which means that small wavelengths are more scattered by small obstacles than higher wavelengths.

Lambert's law for a scattering surface

Lambert's law comes from optics and is deducted from observation of scattering by surfaces. It shows that scattering signal is directly proportional to the cosine of the angle θ between the observer's line of sight and the surface normal. The law is also known as the cosine emission law, or Lambert's emission law. In this case, one speaks of *Lambertian* surfaces. It is named after Johann Heinrich Lambert, from his *Photometria*, published in 1760.

This type of scattering is taken into account particularly for analyzing the ocean; for example, scattering from the bottom of the sea, see Urick (1976).

Let us imagine an acoustic wave intercepting the sea bottom at an incidence θ relative to the bottom.

The surface is supposed to be rough; but at a first approximation, we can think of considering the incidence and the horizontal dimension of the surface such that Snell-Descartes law can be applied.

In fact, the dimensions of surface elements relative to acoustic wavelengths can play a fundamental role, and one finds scattering radiation at angle φ relative to the surface such that if I_{inc} is the incident wave intensity, and dS a surface element, the scattered intensity I_{scatt} is found to be

$$I_{\text{scatt}} = \mu\ I_{\text{inc}}\ \sin(\theta)\ \ \sin(\varphi)\text{d}S \tag{3}$$

where μ is a coefficient of proportionality representative of the surface.

Therefore, we can analyze the relative intensity in dB:

$$\begin{aligned} P &= 10\ \log\left(I_{\text{scatt}}/I_{\text{inc}}\right) \\ &= 10\ \log(\mu) + 10\ \log\left(\sin(\theta)\ \sin(\varphi)\right) \end{aligned} \tag{4}$$

which gives for backward scattering ($\varphi = \pi - \theta$).

$$Pb = 10\ \log(\mu) + 10\log\left(\sin\left(\theta\right)^2\right) \tag{5}$$

This shows a variation of intensity proportional to the square of the grazing angle sinus.

In a case where transmission across the ocean bottom would be null, it is found by integration that the backscattering strength would be −5 dB.

In a same way, for a bottom transmitting no energy to the medium below, Marsh (1964) has proposed an alternative formula:

$$P = 10\ \log\left[(\sin\theta)^4 k^3 A^2(K)/\pi\cos\theta\right] \tag{6}$$

where K is a wave number characteristic of the bottom sea roughness, and $A^2(K)$ the bottom-roughness power spectral density.

This expression shows that a rough bottom acts as described by Rayleigh (1878), and it is found that the roughness elements, which contribute to scatter, are related to the incident wave number and the angle θ by the relation $K = 2k\ \cos\ \theta$, which indeed has the same behavior as what is called *Bragg scattering* (from the physician Sir William Henry Bragg in 1912, in diffraction of X-rays and neutrons in crystals): enhanced backscatter due to coherent combination of signals reflected from a rough surface having features with periodic distribution in the direction of wave propagation, and whose spacing is equal to half of the wavelength as projected onto the surface.

Of course, same relationships for ocean surfaces are used for acoustic scatter at soil surfaces. The same methods used for acoustics are applied more generally to electromagnetic and optical waves (from radar and lidar) to get information on surface roughness.

The question of scatter by surface is, however, more complicated since, generally, one part of incident wave is transmitted across the surface, and the transmission depends on surface and subsurface properties; see Urick (1976).

Acoustic turbulent scattering

The theory of sound scattering from locally isotropic and homogeneous turbulence using the *Born approximation* (use of the incident wave in a homogeneous medium to compute the scattered wave) has benefitted from the conjunction between several researches and discoveries in the recent years: discovery of small-scale turbulence statistical behavior by Kolmogorov (1941), scattering experimental validation by Kallistratova (1959), Monin's (1962) calculation of turbulence spectra for velocity and temperature in the scattering cross-section, and some unification of the question of scattering of waves (electromagnetic and acoustical) in a turbulent medium by Batchelor (1957) and Tatarskii (1961).

The acoustic cross-section of acoustic waves in a turbulent, isotropic, and small-scale medium is

$$\begin{aligned} \eta(\theta s) &= 1/8k^4\ \cos^2(\theta s) \\ &\times \left[\Phi_T(ks)/{T_0}^2 + \cos\left(\theta s/2\right)^2 E(ks)/\pi c^2\ ks^2\right] \end{aligned} \tag{7}$$

described in Batchelor (1957) and Tatarskii (1961, 1971), where η is the differential acoustic cross-section or "reflectivity factor," θs is the angle between scattering and transmitter beam axis, k is the incident acoustic wave number, ks the scattering wave number $= 2\ k\ \sin\ (\theta s/2)$ corresponding to Bragg scattering, T_0 is the mean local temperature in °K, and c is the sound speed.

An inaccuracy in the formula for the dependence of scattering was corrected in Tatarskii (1971), due to the results of Kallistratova (1959, 1960); see Kallistratova (2002).

$\Phi_T\,(ks)$ and $E(ks)$ are, respectively, the isotropic three-dimensional spectral densities for temperature (for a dry atmosphere) and for turbulent kinetic energy.

Let us remark that if transmitter and receiver are at the same location (monostatic system of observation), only temperature fluctuation spectra contribute to scattering, and if one considers scattering at 90° angle, no scatter occurs in this direction. In the general case, the two spectra contribute to scatter, and we can say, in this case, that we are using a bistatic configuration of observation, transmitting in one direction and receiving in another.

This formulation of scatter of sound by turbulence has been at the origin of the first Sodar by McAllister (1968). An historical and physical discussion of Sodar development can be found in Brown and Hall (1978), and in Neff and Coulter (1986).

Important points to be added correspond to small-scale turbulence definition and what scales of turbulence are responsible for backscatter are responsible:

1. Turbulence scales correspond to the so-called inertial range of turbulence, which for the atmospheric boundary layer typically corresponds to scales ranging from centimeters up to several meters.
2. Acoustic scales responsible for scatter are related to resonant scattered waves satisfying the Bragg relationship, $\lambda = 2\,\lambda s$.

Conclusion

Scattering is a very important process that takes place in the presence of rigid deformations of small scales in the propagation medium, or in the case of surface irregularities and of random perturbations in the medium. Remote sensing of atmosphere and ocean surfaces, therefore, needs a careful understanding and analysis of both medium properties and scattering processes.

Bibliography

Batchelor, G. K., 1957. Wave scattering due to turbulence. In Sherman, F. S. (eds.), *Symposium on Naval Hydrodynamics*, NASNRC publication, N°515, National Research Council, Washington DC, Vol. 409, p. 430.

Brown, E. H., and Hall, F. F., 1978. Advances in atmospheric acoustics. *Reviews of Geophysics and Space Physics*, **16**(171), 180.

http://mysite.du.edu/~calvert/waves/radiate.htm

Kallistratova, M. A., 1959. Procedure for investigating sound scattering in the atmosphere. *Soviet Physics-Acoustics*, **5**(512), 514. English translation.

Kallistratova, M. A., 1962. Experimental studies of sound wave scattering in the atmosphere. In *Proceedings of the Third International Congress on Acoustics*. Amsterdam: EAA, ASA, DEGA, Vol. 7, p. 10.

Kallistratova, M. A., 2002. Acoustic waves in the turbulent atmosphere: a review. *Journal of Atmospheric and Oceanic Technology*, **1139**, 1150.

Kolmogorov, A. N., 1941. Dissipation of energy in locally isotropic turbulence. *Proceeding of USSR Academy of Sciences*, **32**, 16–18. English translation in *Proceedings of Royal Society of London, Series A* 434, 15 (1991).

Lord Rayleigh, J. W. S., 1878. *Theory of Sound*. London: Macmillan (1st Ed., 1878, 2nd Ed., 1896). See recent Dover edition, 480 pp.

Lord Rayleigh, J. W. S., 1945. *Theory of Sound*. New York: Dover, p. 480.

Marsh, H. W., 1964. Sea surface statistics deduced from underwater sound measurement. *Annals of the New York Academy of Sciences*, **118**(2), 137–145, doi:10.1111/j.1749-6632.1964.tb33977.x.

McAllister, L. G., 1968. Acoustic sounding of the lower atmosphere. *Journal of Atmospheric and Solar-Terrestrial Physics*, **30**, 1439–1440.

Monin, A. S., 1962. Charcteristics of the scattering of sound in a turbulent atmosphere. *Soviet Physics-Acoustics*, **7**, 370–373. English translation.

Neff, W. D., and Coulter, R., 1986. Acoustic remote sensing. In Lenschow, D. (ed.), *Probing the Atmospheric Boundary Layer*. London: American Meteorological Society, Vol. 201, p. 242.

Tatarskii, V. I., 1961. *Wave Propagation in a Turbulent Medium* (trans: Silverman, R.A.). New-York: Mac Graw Hill, 285 pp.

Tatarskii, V. I., 1971. The effects of the turbulent atmosphere on wave propagation. In *Israel Program for Scientific Translations, Jerusalem*, NTIS TT 68–50464, 472 pp. (Available from the National Technical Information Service, 5285 Port Royal Rd., Springfield, VA 22161).

Urick, R. J., 1976. *Principles of Underwater Sound*. New York: McGraw-Hill, 423 pp.

AEROSOLS

Ralph Kahn
NASA Goddard Space Flight Center
Greenbelt, MD, USA

Synonyms

Airborne particles; Dust; Particles; Particulate matter; PM; Smoke

Definition

Aerosols are solid or liquid particles suspended in the air, typically smaller in size than a twentieth the thickness of a human hair. There is a subtlety: In traditional aerosol science, "aerosol" refers to the particles and the medium in which they are suspended, whereas in remote sensing, the term often refers to just the particles. We use here the latter definition.

Introduction

Aerosols are of interest due to their impact on climate and health, as well as the role they might play in transporting nutrients and even disease vectors on planetary scales. Particles ranging in diameter from about 0.05 to 10 μm are studied most commonly, as they dominate aerosol direct interaction with sunlight, and are also thought to make up the majority of the aerosol mass. The particles are produced naturally by forest and grassland fires, volcanoes, desert winds, breaking waves, and emissions from living vegetation. Human activities, such as fossil fuel and agricultural burning and altering natural land surface cover, are estimated to contribute about 10 % to the global aerosol load, though these tend to concentrate near population centers where they can have both acute and long-term health consequences.

Aerosols are especially challenging to study because they originate from many, diverse sources and exhibit an enormous range of chemical compositions and physical properties. Unlike long-lived atmospheric gases, airborne particles are typically removed from the troposphere by precipitation or gravitational settling within about a week, so aerosol amount and type vary dramatically on many spatial and temporal scales. For this reason, the frequent global coverage

provided by space-based remote sensing instruments has played a central role in the study of aerosols.

Aerosol remote sensing: the first global observations

The aerosol parameter most commonly derived from remote sensing data is aerosol optical depth. It is a measure of aerosol amount based on the fraction of incident light that is either scattered or absorbed by the particles. Formally, aerosol optical depth is a dimensionless quantity, the product of the particle number concentration, the particle-average extinction cross section (which accounts for particle scattering + absorption), and the path length through the atmosphere. It is usually measured along a vertical path. Particle physical and chemical properties, such as size, brightness, and composition, must also be either measured or assumed, to assess aerosol impact on climate and health. Measuring particle properties remotely remains a major challenge to the field.

Since late 1978, the Advanced Very High Resolution Radiometer (AVHRR) imagers have been collecting daily, global, multispectral data, from polar orbit. These instruments were designed primarily to observe Earth's surface, and data analysis typically included an "atmospheric correction" aimed at eliminating surface feature blurring caused by the intervening gas and particles. However, over-ocean, total-column aerosol optical depth was also deduced, initially from single-channel observations, assuming a completely dark ocean surface in the red band (0.63 μm wavelength) and medium-sized, purely scattering particles.

Global, seasonal, and shorter-term aerosol distributions have been mapped. By associating observed particle concentrations with deserts, wildfire regions, and high-population areas on nearby land, dust, smoke, and aerosol pollution plumes were identified. The AVHRR maps showed that Saharan dust is routinely carried across the Atlantic Ocean and deposited in the Caribbean and, more generally, demonstrated the degree to which aerosols are carried long distances. The observations led to interest in the possible impact of aerosols on the energy balance and hence the climate of the planet, and the role desert dust might play in fertilizing iron-poor remote oceans and the Amazon basin.

Among the limitations of this early work was the inability to separate surface from atmospheric contributions to the observed scene brightness, which precluded retrievals over brighter coastal regions and most land. There was also a lack of direct information about particle properties in these retrievals, and an absence of constraints on vertical distribution, both of which are important for calculating aerosol impacts on climate and health. In addition, it was difficult to distinguish cloud from aerosol signals and, more generally, to assess the accuracy of the reported values. Enormous efforts and considerable progress were made in each of these areas over the subsequent 25 years.

One way to avoid significant surface contributions to the observed signal is to view the planet edge on, as was done by the Stratospheric Aerosol and Gas Experiment (SAGE) instruments, beginning in 1979. Observing the sun through the long slant path of the atmosphere as the satellite crossed to the night side of Earth, SAGE produced upper atmosphere vertical soundings, which proved immensely effective for monitoring the sulfate aerosols produced in the stratosphere by the Mt. Pinatubo eruption in 1991. But with no more than two occultations per orbit (about 30 per day), and limited ability to sound even as far down as the upper troposphere, other approaches were needed to address key aerosol-related climate and health questions.

Due to the intense scattering of ultraviolet (UV) light by atmospheric molecules, the surface is obscured when viewed from space in the wavelength range 330–380 nm. In the late 1990s, it was realized that the Total Ozone Mapping Spectrometers (TOMS), versions of which had already been orbiting for nearly 20 years, contained the spectral channels needed to retrieve aerosol amount over land as well as water, based on their ability to absorb the upwelling background UV light. This resulted in the Aerosol Index, a qualitative measure of UV-absorbing aerosols such as dust and smoke. The retrieval has limited sensitivity to near-surface aerosols and depends sensitively on the elevation of the particles and their optical properties, but the maps provided the first comprehensive, long-term record of aerosol source regions and overland transports.

One of the first and most widely used aerosol remote sensing techniques is surface-based sun photometry, which involves measuring the varying intensity of the solar disk as the sun changes elevation in the sky. The method predates satellite observations and relies on observing a systematic increase in atmospheric opacity (and the corresponding decrease in solar brightness) as the sun is viewed through longer atmospheric slant paths. Assuming aerosol horizontal homogeneity, column-integrated aerosol optical depth is retrieved, and if this is done at multiple wavelengths, some information about particle size can also be derived.

Beginning in 1991, with the European Space Agency (ESA) two-view-angle Along Track Scanning Radiometer (ATSR) series of imagers exploited the geometrically based approach from space. Unlike sun photometry, the satellite technique measures light scattered by the scene below, so additional assumptions about aerosol and surface optical properties are required to retrieve column-integrated aerosol optical depth. But the atmospheric contribution to the signal still increases systematically, relative to that of the surface, as the slant path increases, making surface-atmosphere separation possible. The steeper slant paths also improve sensitivity to thinner aerosol layers.

In 1996, the first of the French Space Agency (CNES) POLarization and Directionality of Earth's Reflectance (POLDER) imagers began collecting multi-angle, multispectral polarization data from orbit. The polarization effects of many types of land surfaces are fairly independent of wavelength, making it possible to separate the more constant surface polarization contribution to the satellite signal from the spectrally varying atmospheric contribution. Aerosols are sometimes divided into two groups, depending on whether their effective diameter is greater or less than a certain size, usually taken to be around 1 μm for satellite observations and 2.5 μm for many health and direct sampling applications. The majority of smoke and aerosol pollution particles, the products of combustion and chemical processing, tend to fall into the smaller or "fine" mode. Mechanically produced desert dust and sea salt particles tend to be weighted toward the "coarse" mode. From its combination of optical measurements, POLDER maps column-integrated fine-mode and total aerosol optical depth over water, as well as fine-mode optical depth overland, and more advanced retrieval algorithms for POLDER data are under development.

Second-generation global measurements

The NASA Earth Observing System's (EOS) Terra satellite, launched in late 1999 into a sun-synchronous orbit crossing the equator at about 10:30 local time, carries two instruments designed in part to make detailed aerosol measurements: the MODerate resolution Imaging Spectroradiometer (MODIS) and the Multi-angle Imaging SpectroRadiometer (MISR). MODIS follows the multispectral approach of the AVHRR instruments, but with higher spatial resolution (a maximum of 250 m, compared with up to 1 km for AVHRR), 36 spectral channels, and much higher radiometric calibration accuracy and stability. Total-column aerosol optical depth over global water as well as darker land surfaces is produced routinely every 2 days, along with fine-mode fraction over ocean. Thermal infrared channels are used to detect fires, which can help identify smoke plumes. Efforts are being made to extend the interpretation of MODIS data, for example, by using blue-band data to retrieve aerosol optical depth over bright surfaces (following the TOMS approach) and by developing semiempirical ways of deducing aerosol type from the combination of geographic location, season, and fine-mode fraction. A second copy of MODIS, flying on the EOS Aqua satellite, provides observations similar to MODIS/Terra, at about 1:30 equator crossing time.

MISR complements MODIS, acquiring four-channel, near-simultaneous multispectral views of Earth at nine angles and spatial sampling up to 275 m/pixel. Having a narrower swath than MODIS, MISR takes about a week to image the entire planet. With the multi-angle coverage, aerosol optical depth as well as surface reflectance are retrieved, even over bright desert surfaces. The nine views also sample light scattered in different directions, which yields some information about column-averaged particle size, shape, and brightness under good retrieval conditions; taken together, the retrieved information makes it possible to map aerosol air mass types, though not detailed particle microphysical properties. From the stereo viewing, MISR also derives the heights of clouds and aerosol plumes near their sources. The injection heights of wildfire smoke, volcanic effluent, and desert dust, produced by stereo imaging, are key quantities used in computer-based aerosol transport simulation models to predict plume evolution and aerosol climate impact.

The most accurate information about aerosol vertical distribution is obtained from lidars, which, unlike passive imagers that collect scattered sunlight, send out their own laser beam as the illumination source. Their ability to detect multiple, very thin aerosol layers, day and night, makes it possible for them to create a global, climatological picture of transported aerosols. But the lidar swath is the width of the laser beam, less than a 100 m in size, so coverage of specific sites or events is serendipitous. The technique was demonstrated in 1994, with the Lidar In-Space Technology Experiment (LITE) aboard NASA's Space Shuttle Discovery, and has been followed by the Geoscience Laser Altimeter System (GLAS) and Cloud-Aerosol Lidar and Infrared Pathfinder Satellite Observation (CALIPSO) instruments on polar-orbiting EOS satellites. CALIPSO flies in a constellation of satellites called the "A-Train," aimed at making complementary, near-coincident measurements. It includes Aqua carrying one MODIS instrument as well as PARASOL, and the Aura satellite bearing updated versions of POLDER and TOMS, respectively.

The second-generation measurements also represent a new era for assessing the accuracy of satellite aerosol retrieval results. Surface-based networks of autonomous sun photometers, such as the several-hundred-instrument AErosol RObotic NETwork (AERONET) federation, began producing very accurate, uniformly processed time series of aerosol column amount. The results are compared statistically and event by event with the satellite retrievals. By scanning across the sky in addition to making direct sun measurements, the surface stations collect the data needed to derive column-average particle size and brightness as well. Regional surface-based networks of radiometers also contribute to satellite retrieval validation, as well as surface lidar networks such as the NASA's Micro Pulse Lidar Network (MPLNET) and European Aerosol Research LIdar Network (EARLINet).

Despite enormous advances in space-and ground-based aerosol remote sensing, some key measurements elude these techniques. Currently, detailed knowledge of particle composition, brightness, shape, and ability to absorb water is obtained only by collecting samples of the particles themselves. For near-surface aerosols such as urban pollution particles, surface stations are usually deployed, equipped to measure particle size and mass and to acquire samples for chemical analysis. But for more complete

atmospheric characterization, intensive field campaigns are required, involving aircraft, satellites, and ground stations making coordinated observations, often with the help of predictions from aerosol transport models.

Aerosol environmental effects

Most aerosols scatter more than 90 % of the visible light falling upon them, whereas nearly 70 % of Earth's surface is dark water. So overall, aerosols tend to cool the planet by making it more reflecting than it would otherwise be. Climate models play a central role in assessing the magnitude of this effect, as polar-orbiting satellites provide only snapshots of aerosol optical depth and limited information about their brightness, and aerosol data from geostationary satellites, which can make continuous observations of the sub-spacecraft region, are currently only qualitative. For radiative forcing calculations, models simulate the full diurnal cycle, along with uniform, global fields of aerosol amount, brightness, and vertical distribution. Remote sensing observations provide constraints on these models.

Current assessments suggest that the globally averaged aerosol direct radiative effect amounts to a cooling of about 0.1–0.9 W/m^2, compared to the global warming by carbon dioxide of about 1.66 W/m^2 (IPCC, 2007). Although the aerosol cooling might offset some greenhouse warming, aerosols, unlike long-lived greenhouse gases, are not distributed uniformly, so their regional effects are far more significant than the global mean. Preliminary assessments of observed trends in aerosol optical depth suggest that since the mid-1990s, aerosol particle pollution has decreased over Europe and eastern North America, whereas it has increased over east and south Asia, and on average, the atmospheric concentration of low-latitude smoke particles has also increased.

In addition to the direct effect they have on sunlight, aerosols play a role in the formation of clouds. Collecting the water molecules needed to make cloud droplets is accomplished with the help of aerosols, called cloud condensation nuclei (CCN). The concentration of CCN in the droplet-formation regions of clouds mediates the number of droplets that form. If a fixed amount of cloud water is divided into more droplets of smaller size, the overall reflectivity of the cloud will be greater. The "first indirect effect" of aerosols on clouds refers to the way increased CCN can lead to increased cloud reflectivity. As smaller-sized droplets are less likely to coalesce into raindrops and precipitate, smaller droplets can also increase cloud lifetime, increasing global reflectivity and slowing the cycling of water through the atmosphere, a process often called the second indirect effect.

Aerosols can weaken or strengthen clouds in other ways as well. If dark aerosols such as soot or smoke are present, they can absorb sunlight and evaporate cloud droplets. Aerosols dissolved in cloud droplets may postpone freezing as droplets are carried aloft in the cores of some types of clouds, invigorating their development. Phytoplankton in ocean surface water might actively regulate cloud amount by modulating their output of gaseous sulfur compounds, which in turn form sulfate aerosols in the atmosphere and serve as CCN in aerosol-poor skies over remote oceans. It is difficult to test these hypotheses on large scales with currently available measurements, and therefore to assess their environmental impacts, but observations indicate that such mechanisms must at least be considered as part of the global picture.

The magnitude of aerosol indirect effects on clouds is much less certain that that of aerosol direct radiative effects, in part because detailed particle size and composition, which determine their ability to absorb water, cannot be measured remotely with sufficient accuracy. In addition, most CCN are smaller than 0.05 μm, too small to be distinguished from atmospheric gas molecules by remote sensing techniques. The current consensus model-based estimate for global-average indirect effects is cooling of 0.3–1.8 W/m^2, but with low confidence (IPCC, 2007). Narrowing the uncertainties is likely to require a combination of detailed chemistry and microphysics from aircraft measurements, satellite observations to provide broad statistical sampling, and modeling to generate an overall result.

To date, remote sensing has contributed to our knowledge of aerosol impacts on human health only qualitatively, identifying, with the help of aerosol transport models or lidar profiles, regions where near-surface particle concentrations are especially high. Surface stations are typically more effective in isolating the near-surface aerosols that matter most for these studies, and direct samples are required to provide detailed particle size and chemical composition. However, the spatial coverage of surface stations is very limited. As with climate effects, the future seems to point toward combining satellite and suborbital measurements with models.

Summary

Our appreciation of aerosols' role in climate change has grown over the past 25 years, in part due to the contributions made by remote sensing. First estimates of the impacts transported aerosols have on the atmospheric energy balance, on clouds and the hydrological cycle, on larger-scale atmospheric circulation, and on human health have been made. An understanding has developed for the need to combine detailed physical and chemical measurements from aircraft and ground stations and extensive constraints on aerosol optical depth, type, and vertical distribution from satellites, with numerical models that can simulate present and predict future conditions.

However, much remains to be done. For planning purposes, the accuracy of measurements needed to assess aerosol direct radiative effect must be improved, and uncertainties in aerosol indirect effects on clouds must be reduced. Techniques for systematically constraining models with satellite and suborbital data need to be developed, both to test model parameterizations of aerosol sources, cloud processes, etc., and to assess the

uncertainties in the resulting simulations. Based on past experience, this can be achieved, provided we continue to develop and deploy the instruments, improve the models, and maintain the research community, which have carried the field to this point.

Bibliography

Charlson, R. J., Lovelock, J. E., Andreae, M. O., and Warren, S. G., 1987. Ocean phytoplankton, atmospheric sulphur, cloud albedo, and climate. *Nature*, **326**, 655–661.

Haywood, J., and Boucher, O., 2000. Estimates of the direct and indirect radiative forcing due to tropospheric aerosols: a review. *Reviews of Geophysics*, **34**, 513–543.

IPCC, 2007. The physical science basis. In Solomon, S., Qin, D., Manning, H., Chen, Z., Marquis, M., Averyt, K., Tignor, M., Miller, H. (eds.), *Contribution of Working Group I to the Fourth Assessment Report of the Intergovernmental Panel on Climate Change*. Cambridge: Cambridge University Press.

Kahn, R. A., 2012. Reducing the uncertainties in direct aerosol radiative forcing. *Surveys in Geophysics*, **33**, 701–721, doi:10.1007/s10712-011-9153-z.

Kaufman, Y. J., Tanre, D., and Boucher, O., 2002. Satellite view of aerosols in the climate system. *Nature*, **419**, 215–223, doi:10.1038/nature01091.

Ramanathan, V., Crutzen, P. J., Kiehl, J. T., and Rosenfeld, D., 2001. Aerosols, climate, and the hydrological cycle. *Science*, **294**, 2119–2124.

Seinfeld, J. H., and Pandis, S. N., 2006. *Atmospheric Chemistry and Physics*, 2nd edn. New York: Wiley, p. 1203.

AGRICULTURAL EXPANSION AND ABANDONMENT

Jiaguo Qi
Department of Geography/CGCEO, Michigan State University, East Lansing, MI, USA

Synonyms

Agricultural abandonment; Agricultural expansion; Agricultural land; Change detection; Crop phenology; Mapping agricultural lands

Definition

Agricultural land. Agricultural land may be defined broadly as land used primarily for the production of food and fiber, including croplands, pastures, orchards, groves, vineyards, nurseries, ornamental horticultural areas, confined feeding operations, and other agricultural applications.

Agricultural expansion. The conversion of nonagricultural land use to agricultural use.

Agricultural abandonment. The conversion of agricultural land use to nonagricultural use.

Change detection. The process of identifying and documenting changes in land use over time.

Crop phenology. The study of changes in plant physiology and crop growth stages as influenced by environmental and anthropogenic drivers, including, for example, seasonal variations in temperature and precipitation.

Mapping agricultural lands. Interpreting remotely sensed imagery to categorize agricultural lands.

Introduction

Agricultural lands are by far the largest land areas that have been intensively managed for food and fiber production. Increases in food and fiber demand have driven significant agricultural expansion over the past decades. The rate and magnitude of agricultural expansion are ever increasing, especially under the recent pressure to develop sustainable energy sources such as biofuels from agricultural crops. Agricultural expansion is the *conversion* of nonagricultural lands to agricultural lands, for example, conversion of forested lands to crops, wetlands to rice fields or fishponds, or natural grasslands to pastures.

At the same time, agricultural lands in many places have been abandoned as traditional agricultural operation has become either unprofitable or impracticable. Agricultural abandonment can be a result of various factors ranging from natural to human. The natural factors may include climate change, such as decline in rainfall or the occurrence of extended periods of drought or flood, which makes traditional agricultural operation practically impossible. In places where agricultural operations rely heavily or exclusively on irrigation, agricultural abandonment may occur due to salinization or reduction in ground or surface water supplies. In some cases, agricultural abandonment happens solely due to economic pressures such as the conversion of traditional agricultural lands into suburban real estate developments near major cities around the world.

Agricultural expansion or abandonment has significant consequences for the economy and food security (Alexandratos, 1999; De La Torre Ugarte et al., 2003; Walsh et al., 2003) as agriculture is the backbone of food supplies. However, agricultural expansion can cause detrimental effects on nonagricultural terrestrial and aquatic ecosystems (Tilman et al., 2001). These environmental consequences include increased soil erosion, nutrient leaching that pollutes aquatic environments and degrades water quality, reduced water availability for other ecological uses, and changes in biogeochemical processes that impact greenhouse gas emissions and soil carbon sequestration.

Whether through expansion or abandonment, agricultural land uses are being altered, and these changes will affect food security, the environment, and future sustainability. The role of remote sensing in agricultural expansion or abandonment is to provide detailed assessments of the spatial and temporal changes of agricultural and nonagricultural lands. Effective monitoring of agricultural expansion and/or abandonment provides timely information for decision makers, economists, and environmental scientists to objectively assess future food security and environmental consequences.

Remote sensing of agricultural expansion and abandonment

Remote sensing has been used as a cost-effective tool to map the spatial extent of agricultural lands (Hogg, 1986; Hall and Badhwar, 1987; Congalton et al., 1998). With multi-temporal remote sensing, agricultural expansion or abandonment can effectively be mapped through change detection analysis. As such, remote sensing of agricultural expansion or abandonment requires a minimum of two images acquired on different dates covering the period for documenting changes in agricultural lands. Two common approaches are utilized for this application: (1) comparison of separately classified remote sensing imagery from two or more different dates and (2) direct, single classification of multi-date remote sensing imagery. These change detection approaches are used to quantify agricultural expansion and abandonment.

Mapping agricultural lands

Agricultural mapping using remotely sensed imagery is a common practice where observed spectral radiance or reflectance is classified into different land use categories. Techniques often employed include supervised and unsupervised classification using various cluster analyses (Haralick et al., 1970; Wharton, 1982; Singh, 1989; Congalton et al., 1998; Steele, 2000; Lucas et al., 2007; Karjalainen et al., 2008). The fundamentals of these classification techniques rely on the fact that different land cover types or crops have distinct spectral reflectance properties and patterns. By analyzing their spectral properties or spatial patterns, similar agricultural lands or crops can be grouped together as a single class (Haralick et al., 1973; Bischof et al., 1992; Vailaya et al., 1998; Benediktsson and Kanellopoulos, 1999).

A recent improvement in agricultural land mapping involves the use of phenological properties of crops. Crop phenological information can be derived from repeated satellite observations, such as the normalized difference vegetation index, that track the changes in plant growth and physiological stage. Because different crops have different phenological properties, such as number of days to reach maximum growth, they can be effectively identified or mapped by analyzing the time series of remote sensing observations (Haralick et al., 1980; Jakubauskas et al., 2002; Wang and Tenhunen, 2004; Chang et al., 2007; Wardlow et al., 2007; Busetto et al., 2008). Use of phenology for mapping crop types is a relatively new application due to the recent availability of frequent, repeated remote sensing observations.

Change detection and assessment

Commonly used techniques of change detection include (a) multi-temporal composite image analysis, (b) image algebra (e.g., band differencing and band ratioing), (c) post-classification comparison, (d) binary masking, (e) spectral change vector analysis, (f) cross-correlation, (g) visual on-screen digitization, and (h) knowledge-based vision systems (e.g., Singh, 1989; Congalton et al., 1998; Jensen, 2005). For quantitative assessment of agricultural expansion or abandonment, often the post-classification method is used. It requires co-registration and classification of each remotely sensed image. The two classified maps are then compared on a pixel-by-pixel basis using a change detection matrix. This matrix provides quantitative "from-to" land use change information, thereby documenting the total amount of agricultural lands that have either expanded or been abandoned.

Care must be taken for accurate agricultural change detection and assessment. Image processing/interpretation must account for phenological differences of crop systems and differences in spatial resolution, reduce radiometric artifacts from external factors such as atmospheric and substrate conditions, and ensure accurate co-registration of imagery. The accuracy of change detection depends on the effectiveness of all these image processing procedures. Therefore, high-quality image processing and classification is imperative to accurately assess agricultural expansion or abandonment.

Current obstacles to mapping agricultural expansion/abandonment

Agricultural lands are very dynamic, changing rapidly with time. Remote sensing imagery provides information only about the physical attributes of land cover and not on the "purpose" of the lands, or the intentions of the people who manage the lands. For example, forest is a cover type and can be sensed remotely, but whether the forested land is intended for timber harvesting or recreational uses needs to be determined by the owner. A major obstacle in mapping agricultural land use changes is that while remote sensing can identify land cover changes, these changes may not be the result of agricultural land use changes. Successful mapping of agricultural expansion and abandonment is the differentiation of temporary land cover changes (e.g., short-term fallow) from long-term land use changes. Since temporary land cover changes can have the same or similar spectral properties, mapping agricultural expansion or abandonment requires multiple year observations and sufficient ancillary information in order to identify observed changes in land cover as land use changes.

Another obstacle is related to the nature of agricultural lands themselves. Many agricultural crops have similar spectral properties, phenological development, and spatial patterns as nonagricultural cover types. There may be no spectral or spatial pattern differences across these lands even though their uses are different. This can make accurate imagery classification of agricultural expansion/abandonment mapping very difficult.

Conclusion

Agricultural expansion and abandonment is widespread globally and one of the most important forms of land use change. Accurate assessment and monitoring of the rate and spatial extent of expansion and abandonment provides

vital information about the location and availability of agricultural lands for economists, environmentalists, biologists, ecologists, resource managers, and policy makers. Remote sensing provides a cost-effective and repeatable means of mapping and assessing the spatial pattern and rate of change in agricultural land use. With the capabilities of future advanced earth observation systems, such as the *Global Land Observation System* (GLOS) and the *Global Earth Observation System of Systems (GEOSS)*, it is foreseeable that timely information about agricultural expansion and abandonment will become available to a much broader user community.

Bibliography

Alexandratos, N., 1999. World food and agriculture: outlook for the medium and longer term. *PNAS: Proceedings of the National Academy of Sciences*, **96**(11), 5908–5914.

Benediktsson, J. A., and Kanellopoulos, I., 1999. Classification of multisource and hyperspectral data based on decision fusion. *IEEE Transactions on Geoscience and Remote Sensing*, **37**(3), 1367–1377.

Bischof, H., Schneider, W., and Pinz, A. J., 1992. Multispectral classification of landsat-images using neural networks. *IEEE Transaction on Geoscience and Remote Sensing*, **30**(3), 482–490.

Busetto, L., Meroni, M., and Colombo, R., 2008. Combining medium and coarse spatial resolution satellite data to improve the estimation of sub-pixel NDVI time series. *Remote Sensing of Environment*, **112**, 118–131.

Chang, J., Hansen, M. C., Pittman, K., Carroll, M., and DiMiceli, C., 2007. Corn and soybean mapping in the United States using MODIS time-series data sets. *Agronomy Journal*, **99**, 1654–1664.

Congalton, R. G., Balogh, M., Bell, C., Green, K., Milliken, J. A., and Ottman, R., 1998. Mapping and monitoring agricultural crops and other land cover in the Lower Colorado River Basin. *Photogrammetric Engineering and Remote Sensing*, **64**(11), 1075–1118.

De La Torre Ugarte, D., Walsh, M., Shapouri, H., and Slinksy, S., 2003. *The economic impacts of bioenergy crop production on U.S. agriculture*. U.S. Department of Agriculture, Office of the Chief Economist, Agricultural Economic Report 816.

Hall, F. G., and Badhwar, G. D., 1987. Signature-extendable technology: global space-based crop recognition. *IEEE Transactions on Geoscience and Remote Sensing*, **25**(1), 93–103.

Haralick, R. M., Caspall, F., and Simonett, D. S., 1970. Using radar imagery for crop discrimination: a statistical and conditional probability study. *Remote Sensing of Environment*, **1**, 131–142.

Haralick, R. M., Shanmugam, K., and Dinstein, I., 1973. Textural features for image classification. *IEEE Transactions on Systems, Man, and Cybernetics*, **3**(6), 610–621.

Haralick, R. M., Hlavka, C. A., Yokoyama, R., and Carlyle, S. M., 1980. Spectral-temporal classification using vegetation phenology. *IEEE Transactions on Geoscience and Remote Sensing*, **18**(2), 167–174.

Hogg, H., 1986. Agriculture and resource inventory survey through aerospace remote sensing (AgRISTARS). *IEEE Transactions on Geoscience and Remote Sensing*, **24**(1), 185.

Jakubauskas, M. E., Legates, D. R., and Kastens, J. H., 2002. Crop identification using harmonic analysis of time-series AVHRR NDVI data. *Computers and Electronics in Agriculture*, **37**, 127–139.

Jensen, J. R., 2005. Digital change detection. In Jensen, J. R. (ed.), *Introductory Digital Image Processing: A Remote Sensing Perspective*. Englewood Cliffs: Prentice-Hall, pp. 467–494.

Karjalainen, M., Kaartinen, H., and Hyypp, J., 2008. Agricultural monitoring using Envisat alternating polarization SAR images. *Photogrammetric Engineering and Remote Sensing*, **74**(1), 117–128.

Lucas, R., Rowlands, A., Brown, A., Keyworth, S., and Bunting, P., 2007. Rule-based classification of multi-temporal satellite imagery for habitat and agricultural land cover mapping. *ISPRS Journal of Photogrammetry and Remote Sensing*, **62**(3), 165–185.

Singh, A., 1989. Review article digital change detection techniques using remotely-sensed data. *International Journal of Remote Sensing*, **10**(6), 989–1003.

Steele, B. M., 2000. Combining multiple classifiers. An application using spatial and remotely sensed information for land cover type mapping. *Remote Sensing of Environment*, **74**(3), 545–556.

Tilman, D., 1999. Global environmental impacts of agricultural expansion: the need for sustainable and efficient practices. *Proceedings of the National Academy of Sciences*, **96**(11), 5995–6000.

Tilman, D., Fargione, J., Wolff, B., and d'Antonio, C., 2001. Forecasting agriculturally driven global environmental change. *Science*, **292**, 281–284.

Vailaya, A., Jain, A., Zhang, H. J., 1998. On image classification: city versus landscape. In *IEEE Workshop on Content – Based Access of Image and Video Libraries (CBAIVL)*, Santa Barbara, CA, p. 3.

Walsh, M., De La Torre, U. D., Shapouri, H., and Slinsky, S., 2003. The economic impacts of bioenergy crop production on U.S. Agriculture. *Environmental and Resource Economics*, **24**, 313–333.

Wang, Q., and Tenhunen, J. D., 2004. Vegetation mapping with multitemporal NDVI in North Eastern China Transect (NECT). *International Journal of Applied Earth Observation and Geoinformation*, **6**, 17–31.

Wardlow, B. D., Egbert, S. L., and Kastens, J. H., 2007. Analysis of time-series MODIS 250 m vegetation index data for crop classification in the U.S. Central Great Plains. *Remote Sensing of Environment*, **108**, 290–310.

Wharton, S. W., 1982. A contextual classification method for recognizing land use patterns in high resolution remotely sensed data. *Pattern Recognition*, **15**(4), 317–324.

Cross-references

Agriculture and Remote Sensing
Data Processing, SAR Sensors
Global Earth Observation System of Systems (GEOSS)
Global Land Observing System
Vegetation Phenology

AGRICULTURE AND REMOTE SENSING

Jerry Hatfield[1] and Susan Moran[2]
[1]National Laboratory for Agriculture and the Environment, Ames, IA, USA
[2]USDA ARS Southwest Watershed Research Center, Tuscon, AZ, USA

Definition

Reflectance. Light that is returned from the surface of an object in the same wavelength that impinged on the object.

Emittance. Emission of energy in wavelengths determined by the Stefan-Boltzmann relationship.
Vegetative index. Combination of wavelengths that are related to a specific canopy parameter.
Canopy parameters. Descriptions of factors that physically define the canopy, e.g., height, leaf area, biomass, yield.
Thermal index. Comparisons of canopy and air temperature that are related to crop water deficits.

Introduction

Agricultural scientists have used remote sensing for hundreds of years to observe plants to assess their vigor or stress from a multitude of factors. These original observations were not made with sensors but with the eye that determined the health of the plant. The calibration process was to compare the affected plant against a standard that the individual had observed before and deemed to be healthy. This type of analysis was possible because there was a change in the color of the leaf which the eye detected as a change from normal and thus different from what was expected. Visual observations remain a viable tool for crop assessment.

Remote sensing in agriculture is possible because of the changes in leaf reflectance throughout the visible, near-infrared, and shortwave infrared wavelengths as shown in Fig. 1. A healthy leaf has a larger reflectance in the green portion of the spectrum with smaller reflectances in the blue and red portions. Leaves are unique in that their reflectance rapidly increases near 0.7 μm and remains high throughout the near-infrared region (Fig. 1). These changes in reflectance allow the leaf to avoid the absorption of large amounts of energy that it would have to dissipate through some means of energy exchange. Light absorbed in the visible regions drives the photosynthetic process. Leaves appear green to our eyes because these wavelengths have the highest reflectance. If our eyes could "see" in the near-infrared wavelengths, leaves would appear extremely bright because of the high reflectance. Deviations from the expected patterns provide an indication of some level of stress.

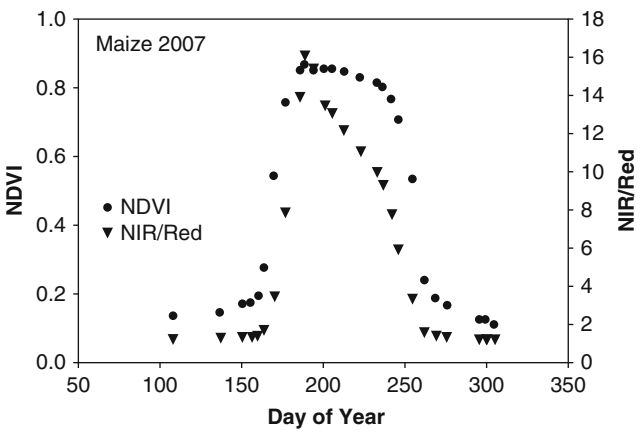

Agriculture and Remote Sensing, Figure 1 Reflectance of an individual leaf in the visible and near-infrared portions of the light spectrum.

The use of spectrophotometers to measure the optical properties of leaves were presented in the early work by William Allen, David Gates, Harold Gausman, and Joseph Woolley who described the basic theory relating morphological characteristics of crop plants to their optical properties (Allen et al., 1969; Gates et al., 1965; Gausman et al., 1969; Woolley, 1971). Their efforts provided detail about high-resolution spectral signatures of natural and cultivated species and were sources of information about normal plant growth and conditions caused by nutrient deficiency, pests, and abiotic stresses (Gausman and Allen, 1973). These research findings help describe, for the first time, the reasons why the spectral signatures of leaves varied from the expected values and the information contained by examining these deviations. Through these basic studies the foundation was formed for what is applied today as remote sensing tools for agriculture. It is not possible to list all of the publications generated by these pioneers in remote sensing but their efforts help develop the basic understanding of leaf reflectance that is utilized today in remote sensing of agricultural crops.

Leaves are not the same as plant canopies and reflectance values for canopies are more complex than individual leaves. Canopies have many different morphological forms because of branch arrangement on trees and vines, leaf architecture and positioning on annual and perennial plants, whether plants are deciduous or evergreen, and how plants are arranged in different planting configurations. Observations of different plants provide an indication of how different canopies reflect light. There is a vast array of potential shapes of canopies, and light interactions with canopies are different than individual leaves. It is this interaction of light with plant canopies that has provided for the value of remote sensing of agricultural canopies and the potential value for using reflectance from different canopies to assess various canopy properties.

The thermal portion of the spectrum represents the longwave radiation and the wavelengths emitted are determined by the Stefan-Boltzmann relationship in which the wavelengths emitted are function of the fourth power of the temperature of the object. Objects on the earth's surface emit in wavelengths between 8 and 14 μm because of their temperatures being in the range of 300 K. Remote sensing of crop surfaces using infrared thermometers has become routine and offers the potential for crop water stress detection and water management. Similar to the visible and near-infrared research, understanding the importance of thermal radiation for agricultural crops can be traced to original observations by Tanner (1963) who found that plant temperature varied from air temperature and could be measured with thermocouples attached to the leaves. Since that basic discovery, there have been continual advances in the use of thermal wavelengths in agricultural applications.

There has been considerable progress in the field of remote sensing and agriculture and the progress was recently documented in Volume 69 of *Photogrammetric Engineering and Remote Sensing* in 2003. The topics covered in this volume were sensor techniques (Barnes et al., 2003), hydrometeorological applications (Kustas et al., 2003), crop management applications (Pinter et al., 2003), crop yield assessment (Doraiswamy et al., 2003), applications to rangeland assessment and management (Hunt et al., 2003), water quality assessment (Ritchie et al., 2003), and sensor development and correction methods (Moran et al., 2003). Another recent review of the application of remote sensing methods to dryland crops was developed by Hatfield et al. (2004) and the advances of remote sensing to agronomic decisions by Hatfield et al. (2008).

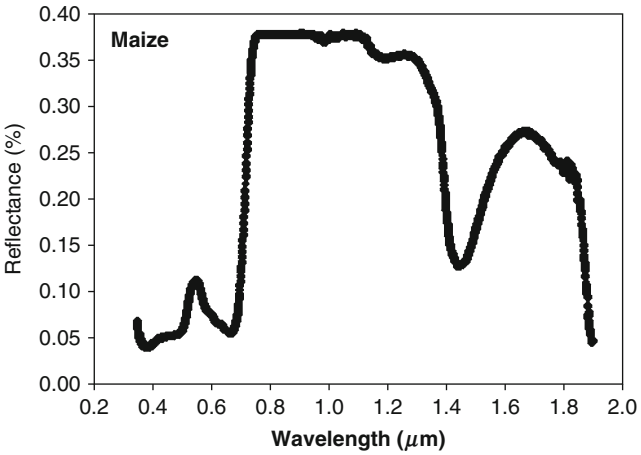

Agriculture and Remote Sensing, Figure 2 Reflectance across the visible and near-infrared portions of the spectrum for a corn canopy across the year.

Canopy parameters

Observations of canopies provide information about the typical parameters that are observed through other means. These include biomass, leaf area, ground cover, chlorophyll content of the canopies, light interception, grain yield, and crop residue on the soil surface. Each of these parameters provides critical information that can be used to determine if the progression of the crop is at a normal rate or is deviating either in a negative or positive direction away from the normal expectations. It is important to detect how quickly the crop is developing during the season and the size of the plant.

Canopies change throughout the growing season and it is that change that provides the information that can be detected from remote sensing platforms. Agricultural canopies vary in their size, row direction, canopy shape, and even color. Annual crops are different from perennial crops such as orchards or vineyards. Agricultural systems like pastures or rangelands that are permanent grasses or shrubs display large changes throughout the year. It is important to realize that each crop is different, and crop identification has been a primary goal of many remote sensing studies. These crop identification approaches have been used to develop land use maps and crop area for the earth's land area.

Canopy reflectance is different from leaves because of the soil background beneath the crop. Canopy reflectance varies throughout the year, and if we apply the spectral maps to a whole canopy, as compared to an individual leaf, remarkable differences can be observed, as shown in Fig. 2 for a corn crop. There are several important features in this figure that reveal information about the canopy. First, the reflectance of bare soil when there is no canopy is linear and exhibits little difference among individual wavelengths. Second, the variation in the reflectance values for the bare soil is caused by changes in surface roughness induced by either tillage or rainfall events. Third, there is a rapid change in the reflectance values in the visible and near-infrared portions as the canopy begins to develop and grow. Coupled with the rapid increase in the near-infrared reflectance values, there is a concurrent decrease in the blue and red and an increase in the green wavelengths. Fourth, there is an equally rapid decline in the near-infrared reflectances as the canopy begins to senesce and the green leaves turn brown. There are very dynamic changes that occur throughout the growing season and these dynamics provide the potential information content from tracking the reflectance patterns of different wavelengths.

Vegetative indices

Vegetative indices (VIs) has been used as a term that describes the relationship of a combination of wavebands or wavelengths to a particular canopy parameter. These VIs range from simple ratios of wavebands to complex empirical relationships of different wavebands or even combinations of different VIs for specific purposes. These have been developed and evaluated extensively over the past 30 years which coincides with the acquisition of reflectance data from the Landsat platforms. These satellites were launched with four broad wavebands that have been extensively used in the development and application of a number of VIs. A summary of the different VIs provided by Jackson and Huete (1991) stated the purpose of VIs was to enhance the vegetation signal while minimizing the solar irradiance and soil background effects. The adjustment for soil background effects is extremely critical in using remote sensing because annual crop canopies and many perennial tree crops are planted in rows. Developing crop canopies do not completely cover or shade the soil; therefore, viewing the crop from above presents a problem in which the signal is a mixture of the bare soil reflectance values and the leaf reflectance. The canopy reflectance is a mixture of both surfaces and VIs need to be sensitive to soil background and be able to compensate for these differences.

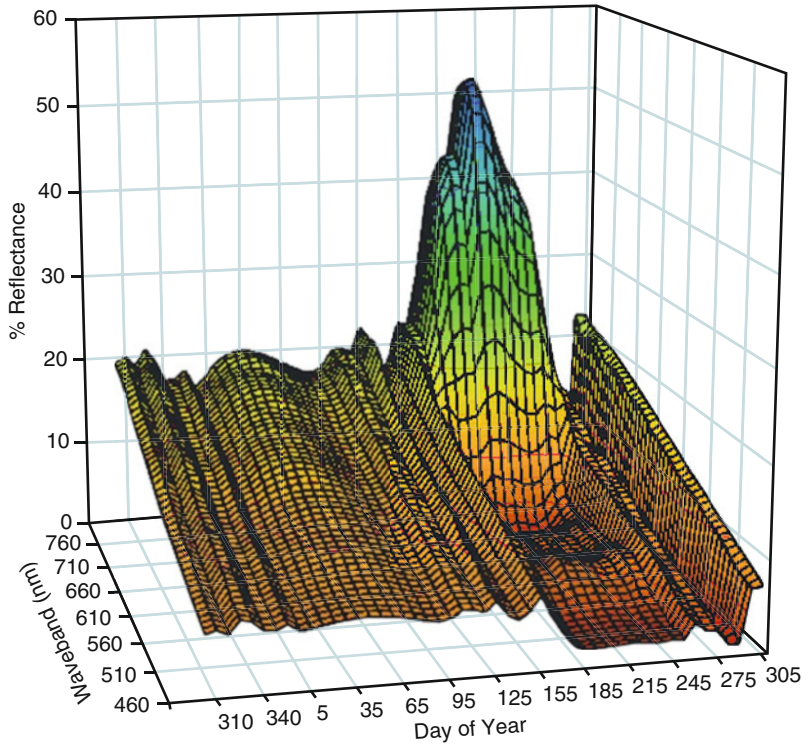

Agriculture and Remote Sensing, Figure 3 Seasonal changes in NIR/RED reflectance and normalized difference vegetative index (NDVI) for a maize canopy in central Iowa.

The development of VIs can be traced back to Jordan (1969) who related the ratio of NIR (0.8 μm) to red (0.675 μm) reflectance (NIR/RED) to leaf area index (LAI). Tucker (1979) found it was possible to use red and near-infrared as measures of changes in vegetation over large areas and increased the confidence that VIs had an application for large-scale assessment of crop canopies. He proposed a difference vegetative index (DVI) as NIR-RED. Development of VIs either as ratios of wavebands or linear combinations of wavebands has been primarily through statistical analyses of observed crop parameters and reflectance data. The seasonal trajectory of reflectance from a crop canopy reveals the red reflectance reaching a minimum with increasing leaf area while the near-infrared (NIR) increases (Fig. 2). This causes the ratio to increase as the canopy develops and a range of NIR/RED values from about 1 to over 20. One of the major limitations in the NIR/RED ratio is the lack of sensitivity when the ground cover is low and both reflectance values are similar. Deering (1978) found this limitation could be overcome through the use of a normalized difference vegetative index (NDVI) as shown in Eq. 1.

$$\mathrm{NDVI} = \frac{\mathrm{NIR} - \mathrm{RED}}{\mathrm{NIR} + \mathrm{RED}} \tag{1}$$

The NDVI has been used extensively for the past 20 years as one of the standard VIs for application to crop canopies. It is important to understand the history of VIs and their limitations that were first proposed by the developers of the index. As an example of these limitations is the application of NDVI to various canopy parameters; however, the seasonal trajectory of this index shows a plateau during the vast portion of the growing season because the index becomes saturated at values between 0.9 and 1.0 and when the leaf area index of the canopy reaches values between 3.5 and 4.0 (Fig. 3). When compared to the NIR/RED ratio, there are differences throughout the growing season. Hatfield et al. (1984) evaluated the relationships between LAI, intercepted photosynthetically active radiation (IPAR), and VIs for durum wheat and found that NDVI and intercepted PAR were strongly related. They found that there were two relationships, one for the stage of accumulating leaf area and one for senescing leaf area. This was the first attempt to bring together the NDVI and intercepted light to explain the nonlinear nature of the NDVI and light interception. The comparison of NDVI across multiple data sets by different investigators was summarized by Hatfield et al. (2004). One of the utilities of this approach is being able to estimate intercepted PAR by crop canopies for use in crop growth models for biomass and yield estimates.

Compensating for the soil background in observations of crop canopies has posed a problem for many of the VIs and several modifications to the VIs have been developed to compensate for the soil background. There have been three forms of VIs developed to address the soil background problem. One of the first was proposed by Kauth and Thomas (1976) and used a linear combination of four wavebands using principal component analyses to estimate brightness, greenness, yellowness, etc. "Brightness" represents the magnitude of the reflected energy and could be considered a soil background line. "Greenness" represents an orthogonal plane to the soil line that contained information about vegetation. "Yellowness" is an additional plane to the soil and vegetation lines with particular sensitivity to senescent vegetation. These three parameters provide information content about plant crop canopies during the course of a growing season.

Another method of addressing the soil background was developed in the form of the perpendicular vegetative index (PVI) proposed by Richardson and Weigand (1977) using a statistical relationship given in Eq. 2.

$$\mathrm{PVI} = (\mathrm{NIR} - a\mathrm{RED} - b)/(1 + a^2)^{1/2} \quad (2)$$

To simplify this relationship, Jackson (1983) proposed that PVI could be expressed as:

$$\mathrm{PVI} = 0.647\mathrm{NIR} - 0.763\mathrm{RED} - 0.02 \quad (3)$$

As a further refinement, Huete (1988) developed ratio-based VIs to account for soil background through an approach he termed "soil-adjusted vegetative index" (SAVI) described as follows:

$$\mathrm{SAVI} = \frac{\mathrm{NIR} - \mathrm{RED}}{\mathrm{NIR} + \mathrm{RED} + L}(1 + L) \quad (4)$$

The L term is an adjustment factor with a value of nearly 0.5 and was added to increase the sensitivity in the separation of canopy and soil at low ground cover amounts. The SAVI index was redefined by Rondeauz et al. (1996) who proposed an optimized SAVI (OSAVI) with the L term set equal to 0.16. Baret et al. (1989) provided an adjustment for soil background to the NDVI as the transformed soil-adjusted vegetative index (TSAVI) described as follows:

$$\mathrm{TSAVI} = \frac{a(\mathrm{NIR} - a\mathrm{RED} - b)}{(\mathrm{RED} + a\mathrm{NIR} - ab)} \quad (5)$$

where a and b represent empirical coefficients obtained by regression fits to observed data. The changes to the VIs to compensate for soil background demonstrate the path that many VIs have taken toward improving the ability to detect differences in canopy responses.

Vegetative indices provide different representations of canopy parameters and there has been an evolution in these indices with the change from broadband to narrow wave band or hyperspectral sensors. In many cases there has been a refinement in the wavelengths used in the VI but not a change in the functional description of the index. A summary of the different VIs and their application is presented by Hatfield et al. (2008).

Application to canopy parameters

Leaf chlorophyll content

The greenness of leaves as indicated by their chlorophyll content has emerged as one of the critical parameters in assessing the status of crop canopies. Leaves contain chlorophyll, Chl *a* and Chl *b*, essential pigments for the conversion of light energy to chemical energy. Solar radiation absorbed by leaves is a function of the photosynthetic pigment content and directly related to photosynthetic potential and primary production. Changes in leaf chlorophyll content are related to plant stress and senescence. One of the emerging applications of leaf chlorophyll observations is the estimation of the nutrient status because leaf nitrogen is incorporated into chlorophyll. There have been handheld chlorophyll absorbance meters developed to measure leaf transmittance at two wavelengths in the red (0.660 μm) and near-infrared (NIR; 0.940 μm) with the theoretical principles of these meters described by Markwell et al. (1995). The principles of the handheld meters have been extended to remote sensing systems that utilize different combinations of wavebands. An example of a canopy-level chlorophyll index is the modified chlorophyll absorption ratio index (MCARI) proposed by Daughtry et al. (2000) as:

$$\mathrm{MCARI} = [(\mathrm{R}_{700} - \mathrm{R}_{670}) - 0.2(\mathrm{R}_{700} - \mathrm{R}_{550})] \times (\mathrm{R}_{700}/\mathrm{R}_{670}) \quad (6)$$

This index was developed using three different wavebands that provide information about the chlorophyll absorption at 0.67 μm relative to the green reflectance peak at 0.55 μm and the near-infrared reflectance at 0.7 μm. Using these three wavebands shows the maximum difference in reflectance for a leaf (Fig. 1). A refinement of the MCARI was proposed by Haboudane et al. (2002) as the transformed chlorophyll absorption ratio index (TCARI) that changed the form of the relationship as shown in Eq. 7:

$$\mathrm{TCARI} = 3[(\mathrm{R}_{700} - \mathrm{R}_{670}) - 0.2(\mathrm{R}_{700} - \mathrm{R}_{550}) \times (\mathrm{R}_{700}/\mathrm{R}_{670})] \quad (7)$$

Gitelson et al. (2003) showed the possibility of methods to estimate chlorophyll content for plants based on simple ratio of NIR/RED reflectance – 1 or $\mathrm{NIR}/\mathrm{RED}_{\mathrm{edge}}$ reflectances – 1 and demonstrated the potential of these for canopy level assessments. The MCARI method was found to be sensitive to leaf area index, chlorophyll, leaf area-chlorophyll interactions, and background reflectance (Daughtry et al., 2000) and was especially sensitive to background reflectances when the canopy leaf area was small. Wu et al. (2008) provided a comparison of different

VIs for their ability to detect chlorophyll contents in winter wheat canopies and found the integrated methods that linked VIs sensitive to soil background (OSAVI) with chlorophyll indices (MCARI or TCARI) were the most robust. The estimation of leaf or canopy-level chlorophyll content provides valuable information about the canopy and potential response to nutrient stress or other stress that affects either Chl *a* or Chl *b* formation within the leaf. Zhang et al. (2008) applied these methods to predict the canopy chlorophyll content per unit ground area using hyperspectral sensors. Feret et al. (2008) combined a leaf optical model with the leaf chlorophyll information and leaf reflectance and transmittance to improve the estimation of chlorophyll content for canopies using remote sensing methods. These types of methods provide information about the canopy and are gaining wider use as a diagnostic tool for remote sensing of crop canopies.

Crop biomass

Crop biomass represents the total aboveground accumulation of plant material and is a tangible form of the net primary productivity of crop canopies. Remote sensing has been used to estimate dry matter accumulation or biomass estimation through a combination of NIR and red wavebands. These empirical fits have plant-specific relationships because of the difference in NIR reflectance among species, and this approach requires calibration for each crop and soil combination. There is a stronger relationship to green biomass with the NIR/RED combinations than to total biomass which includes stems, branches, or other nongreen matter.

Other approaches to estimating crop biomass have been to use a conversion factor of intercepted solar radiation to crop biomass using the following form of the relationship:

$$\text{Biomass} = \int \text{PAR} \bullet \text{fIPAR} \bullet \text{RUE} \bullet \Delta t \tag{8}$$

where PAR is the incident radiation, fIPAR the fraction of intercepted photosynthetically active radiation (PAR) by the canopy, RUE the conversion efficiency of PAR to dry biomass, and Δt the time interval. The estimation of the intercepted values of PAR has taken on many different forms for this approach.

One component of biomass accumulation is the gross primary productivity (GPP) and Gitelson et al. (2006) found that GPP relates closely to total chlorophyll content in maize and soybean. The relationship algorithm for GPP estimation provided accurate estimates of midday GPP in both crops under rainfed and irrigated conditions. This approach has been evaluated using Landsat data to estimate canopy chlorophyll data and photosynthetically active radiation in a combination as proxies for GPP by Gitelson et al. (2012). They found these algorithms were able to estimate GPP accurately at three sites across the Midwest.

Intercepted solar radiation

Estimation of crop biomass is often based on intercepted light by crop canopies and is a critical component in plant growth models. Estimation of light interception by canopies from remotely sensed data would greatly aid in comparing management systems. Intercepted light by a crop canopy can be related to the accumulation of biomass and harvestable grain yield. Daily estimates of intercepted light can be obtained from extrapolation of observations of NDVI combined with daily total PAR obtained from a nearby meteorological station. It is possible to directly compare the performance of different cropping systems using this type of approach with confidence in the results. Observations collected over a wide range of crops and growing conditions suggest that LAI is best obtained from NIR/RED ratios while IPAR is best determined from NDVI.

One of the applications of intercepted light is to determine the rate of senescence of crop canopies. Examination of the rate of change in the NDVI shown in Fig. 3 can be utilized as a tool to examine how quickly plants are losing their physiological functions at the end of the growing season. This approach offers potential to determine if the rates of changes are different than expected and may indicate if there are some factors causing premature loss of green leaves in the canopy. This type of approach is often used for visual determination of premature changes in the canopy and could be easily determined from remote sensing platforms.

Crop ground cover

One of the components that is often evaluated for agricultural applications is the amount of ground covered by the crop canopy and is expressed as the fraction of ground area covered by the projection of standing leaf and stem area onto the ground surface. Changes in ground cover are often indicative of the health of the crop. Determination of ground cover provides a linkage between the growth of the crop and water use patterns of the crop since many evapotranspiration (ET) models use crop cover to relate potential ET to actual ET.

Maas (1998) proposed a method of estimating canopy ground cover in cotton that combined the overall reflectance of the scene and the individual reflectance values from the soil and the crop. He developed the following model for ground cover:

$$GC = (R_{\text{scene}} - R_{\text{soil}})/(R_{\text{canopy}} - R_{\text{soil}}) \tag{9}$$

where GC is the fraction of ground cover, R_{scene} is the scene reflectance, R_{soil} is the soil reflectance, and R_{canopy} is the canopy reflectance. Scene reflectance is expressed as:

$$R_{\text{scene}} = R_{\text{canopy}}GC + R_{\text{soil}}(1 - GC) \tag{10}$$

He used reflectance values from either red (0.6–0.7 μm) or NIR (0.8–0.9 μm) for these relationships and

found that either waveband could be used. This method of estimating ground cover was independent of location and year. This method was not dependent upon empirical fits of the VI with plant parameters. Estimation of ground cover via remote sensing has proven to be fairly simple and not subject to problems associated with LAI or IPAR. The error in estimates of ground cover using these approaches has been on the order of ±5 %. This level of error is acceptable for agricultural applications that require ground cover estimates.

Canopy leaf area index

Estimation of the amount of green leaf area of a crop has been one of the primary approaches to understanding crop growth and development and quantifying the effects of different agronomic practices on crop growth. Leaf area index has been used to assess the ability of a plant to intercept light and LAI is used as one of the critical parameters in crop growth models. The NIR/RED ratio was found to be highly correlated with green LAI. However, there was a different form of the relationship of $\mathrm{LAI} = a + b$ NIR/RED for the growth and senescence portions of the growth cycle. Leaf area estimates for different crops across locations have been summarized by Wiegand and Hatfield (1988) and Wiegand et al. (1990). LAI for wheat was best estimated by the NIR/RED ratio or the TSAVI index using the linear relationships with coefficients of $\mathrm{LAI} = a + b$ NIR/RED and for TSAVI of $\mathrm{LAI} = a + b$ TSVAI. Estimates of LAI are possible with simple linear models using NIR/RED reflectance. However, there is improvement when the same parameters are used but in a different form, with greatly improved sensitivity. These relationships are valid across a number of crops and agronomic practices within and among locations. To be useful for standard agronomic practices, these relationships need to be calibrated for a specific crop. The multisite comparisons for corn, wheat, and grain sorghum provide a degree of confidence that remote sensing measures can be adequately used to estimate LAI.

There is a relationship between LAI and light interception in plant canopies. One approach that has been proposed for estimating LAI is based on the relationships between fractional cover, f_C, and LAI using a relatively simple exponential relationship (Choudhury, 1987):

$$f_C = 1 - \exp(-\beta \mathrm{LAI}) \tag{11}$$

where β is a function of the leaf angle distribution. He estimated β as 0.67 from an average of 18 crops. This method, although robust, has not been applied as often as NIR/RED ratios because the first step in this method is to obtain an estimate of ground cover or fractional cover and then incorporate it into Eq. 11. The multiple steps for this approach have contributed to the more widespread use of the simple regression models between VIs and LAI.

Crop yield

The estimation of green leaf area, intercepted light, or crop biomass is a foundation for the eventual estimation of harvestable crop yield. Yield estimation from remotely sensed data is generally accomplished with either reflectance-based or thermal-based models. These models can be characterized as some form of a relationship between rate of change in the VI and crop growth rate. Considerable variation in the response of the different models across locations has been observed because many of the approaches used empirical fits between yield and remotely sensed data. Deviations from normal grain-filling conditions either by soil, weather, or agronomic practices may not be detectable in simple VI relationships. Grain yields can be related to the rate of crop senescence. Rate of crop senescence can be determined from NDVI or NIR/RED ratios. Crop yield can be estimated from various remote sensing methods and generally involves some method of using the biomass or LAI values obtained from VIs as inputs into either crop growth models to predict yield or direct estimates of yield. Shanahan et al. (2001) used TSAVI, NDVI, and a Green NDVI (GNDVI) where the red reflectance replaced by green reflectance showed an improvement in yield estimation. They found GNDVI provided a slight improvement in yield estimates for the four corn hybrids grown with varying nitrogen (N) and water levels and the utility of this method is the spatial distribution of yield within fields. There continues to be studies reported that relate green, red, NIR, and NDVI values to examine field scale variation in grain yield. In these studies, yield is positively related to NIR and NDVI values and negatively related to green and red values. However, when a comparison is made across the studies there is a large variation in the coefficients in the statistical relationships between VI and grain yield.

There is a need for continued refinement of remote sensing approaches to estimate yield because of the importance in predicting large-scale crop yields or developing field scale maps of yield variation as a part of precision agriculture. One of the areas of potential improvement in yield predictions from remotely sensed observations will occur if we begin to critically evaluate the reasons for the lack of fit between observed and predicted data. Much of the variation can be explained by failure to have field validation data collected at the proper time or incorporation of the improper VIs into these relationships.

Utilization of thermal radiation

Thermal radiation emitted from crop or soil surfaces is representative of the temperature of the surface. However, the utilization of thermally infrared-derived temperatures for assessment of agricultural systems requires a comparison to air temperature. Crop stress methods using surface temperature are based on the comparison with air temperature because of the linkage to the sensible heat exchange of the crop surface. Leaves or canopies that

are cooler than the air temperature have a rapid evaporation rate while those that are warmer than air have a reduced evaporation rate. Plants that have adequate soil water supplies will tend to have leaves cooler than air and as the water supply becomes more limited the leaves will gradually become warmer than the surrounding air. This is premise of all approaches that utilize canopy temperatures that assess crop stress. Unlike the VIs, the use of thermal infrared information has been formed from indices derived from combinations of air and canopy temperatures as empirical relationships to crop yield or biomass based on a comparison to the expected values for a crop in a non-stressed environment. One of the uses of thermal infrared has been the estimation of evapotranspiration from crop canopies.

Variation of the simple canopy: Air temperature difference ($T_c - T_a$) across crops and climates invoked a series of studies that led Idso et al. (1981) to derive an empirical model for canopy stress, while Jackson et al. (1981) derived the more theoretical relationship based on the energy balance of a canopy. The empirical model for CWSI is described as:

$$\mathrm{CWSI} = \frac{\mathrm{d}T - \mathrm{MIN}}{\mathrm{MAX} - \mathrm{MIN}} \tag{12}$$

where $\mathrm{d}T$ is $T_c - T_a$, MIN is the non-stressed baseline given as $a + b$ (Vapor Pressure Deficit, VPD), and MAX the upper limit of $T_c - T_a$ when the canopy is no longer transpiring. Values for MIN are obtained by measuring T_c throughout a day to obtain the data necessary for the regression equation. Values for MAX are constant across a range of VPDs and are observed in studies in which canopies are not completely water-stressed. The more critical relationship to define in Eq. 12 is the non-stressed lower baseline. Jackson et al. (1981) derived these curves from the relationship as follows:

$$\mathrm{CWSI} = 1 - \frac{E}{E_p} = \frac{\gamma\left(1 + \frac{r_c}{r_a}\right) - \gamma\left(1 + \frac{r_{cp}}{r_a}\right)}{\Delta + \gamma\left(1 + \frac{r_c}{r_a}\right)} \tag{13}$$

where the quantity r_c/r_a is expressed as:

$$\frac{r_c}{r_a} = \frac{\frac{r_a R}{\rho c_p} - (T_c - T_a)(\Delta + \gamma) - (e_a^* - e_a)}{\gamma\left[(T_c - T_a) - \frac{r_a R_a}{\rho c_p}\right]} \tag{14}$$

and E is actual evaporation, E_p potential evaporation, r_{cp} the canopy resistance of a well-watered canopy, r_c the actual canopy resistance, r_a the aerodynamic resistance to sensible heat transfer, R_n the net radiation, Δ the slope of saturation curve, γ the psychometric constant, e_a^* the saturation vapor pressure, and e_a the actual vapor pressure of the air. There are differences between Eqs. 13 and 14; however, one can derive the theoretical shape of Eq. 12 from the assumptions of a well-watered and a completely stressed or non-transpiring canopy. Both of these approaches demonstrated the universal application of these relationships. The crop water stress index (CWSI) has become one of the most widely used methods for quantifying crop stress. The efforts to use these approaches have been summarized in Hatfield et al. (2008).

One of the issues with use of canopy temperatures that is similar to using VIs from reflected radiation is the problem of incomplete canopy cover. In the application of canopy temperatures, the problem of incomplete ground cover is more critical because of the potential differences in the temperatures between the soil and the crop. The use of the average temperature based on a fractional ground cover may not provide the correct average compared to the fractional representation of reflectance values. The development of multiscale approaches that combine thermal, visible, and near-infrared imagery from multiple satellites to partition the fluxes between the soil and canopy offer the potential for future improvements in the use of surface temperature at scales ranging from 1 m to 10 km (Anderson et al., 2007). This type of method shows further refinement in the ability to use remote sensing as an assessment tool for ground-based observations as well as a method for regional-scale measurements.

Application to agricultural problems

Crop nutrient status

Estimation of the crop nutrient status is one of the goals of remote sensing and critical to agricultural production because of the need to optimize crop production relative to the nutrient inputs and reduce the potential environmental impacts from agricultural production systems. The detection of chlorophyll content that was discussed earlier has formed the basis for the development of tools to detect either nitrogen or phosphorus stress in crop canopies. There have been studies that have shown that improvements in nutrient management are possible with remote sensing tools that are calibrated to detection of nutrient stress. These efforts will continue to develop and provide valuable information for management decisions.

Pests and other stresses

There are a variety of potential stresses from a variety of other biotic factors. Detection of biotic stresses using remote sensing is not as advanced as the estimation of canopy parameters. There are a few examples of how remote sensing can detect pests. Riedell and Blackmer (1999) found that aphids (*Diuraphis noxia*, Mordvilko) and greenbugs (*Schizaphis graminum*, Rondani) caused changes in the 625–635 μm and 680–695 μm wavebands because of their effect on leaf chlorophyll status. For this approach to effectively detect stress, a comparison would have to be made to a non-stressed plant. One of the merits of this approach is the ability to detect the

presence of aphids in parts of the field because these insects generally do not uniformly affect a field but occur in isolated areas.

Many leaf diseases cause changes in leaf reflectance and many of these observations have been made for a number of years. One of the early reports was by Blazquez and Edwards (1983) who showed it was possible to detect disease occurrence in both tomato and potato leaves using spectral reflectance. Comparisons that relate disease occurrence, timing, and location information are likely to provide some method of discriminating between disease and healthy leaves at the canopy level. Detection of insects and diseases using a combination of spectral signatures has been conducted at the leaf and canopy scale but the routine extension to the field scale has not been demonstrated.

Weeds within canopies provide another source of confusion with remotely sensed data. These effects are unlike insects or diseases because spectral signatures of weed leaves are similar to crop canopies. Medlin et al., (2000) used green (0.535–0.545 μm), red (0.69–0.7 and 0.715–0.725 μm), and NIR (0.835–0.845 μm) wavebands to detect *Ipomoea lacunosa* L., *Senna obtusifolia* (L.) Irwin et Barnaby, and *Solanum carolinense* L. in soybean canopies. They could detect these infestations within the soybean canopy with 75 % accuracy; however, the greatest difficulty was in the detection of weed-free areas in the field. Their ability to detect weeds was due to differences in reflectance for these wavebands between weeds and the crop. Detection of weeds within various crop and rangeland or pasture canopies has been reported for *Ericameria austrotexana* M. Johnst. (Anderson et al., 1993), *Euphorbia esula* L. (Everitt et al., 1995), and *Chrysanthemum leucanthemum* L. (Lass and Callihan, 1997). Other studies have found only limited success in differentiating crops and weeds because of the similarity of spectral reflectance of weeds and crops (Richardson et al., 1985; Menges et al., 1985). They found they were able to detect plant community areas later in the season due to increased ground cover of weed-crop mixture.

Observations for current research suggest two potential avenues for detection of weeds within crop canopies. First is the direct detection of the weed within the crop by separating the spectral signatures for weeds versus crops. Second is the change in field variability patterns because weeds are not evenly distributed across fields and often aggregate in patches across fields similar to detection of insects or diseases within fields. Both of these approaches have not been extensively explored or evaluated with remote sensing tools. The improvements in both the spatial resolution of reflectance data and the temporal frequency provide opportunities for integrated studies of the remote sensing community with agronomists, weed scientists, entomologists, nematologists, and plant pathologists that will provide new techniques for detection of stresses in crop communities.

Conclusions

Remote sensing for agriculture has had a rich history of providing information about crop canopies. The utilization of reflectance data is enhanced through the incorporation into VIs, and the continual refinement of these VIs for application beyond the estimation of canopy parameters will continue to improve the knowledge base of crop changes throughout the year. The utility of remote sensing to move beyond observation to potential field-scale management by providing more detailed information on the spatial patterns within fields and the value of that information will increase the richness of the data and increase the value for the producer. Increasing the application of these relationships for all crops beyond the agronomic systems and into vegetables, vines, and fruits will require improved understanding of the relationships between reflectance and emittance and canopy parameters. This field continues to evolve and offers the potential for many new areas of investigation.

Bibliography

Allen, W. A., Gausman, H. W., Richardson, A. J., and Thomas, J. R., 1969. Interaction of isotropic light with a compact plant leaf. *Journal of the Optical Society of America*, **59**, 1376–1379.

Anderson, G. L., Everitt, J. H., Richardson, A. J., and Escobar, D. E., 1993. Using satellite data to map false broomweed (*Ericameria austrotexana*) infestations on south Texas rangelands. *Weed Technology*, **7**, 865–871.

Anderson, M. C., Kustas, W. P., and Norman, J. M., 2007. Upscaling flux observations from local to continental scales using thermal remote sensing. *Agronomy Journal*, **99**, 240–254.

Baret, F., Guyot, G., and Major, D. J., 1989. TSAVI: a vegetation index which minimizes soil brightness effects on LAI and APAR estimation. In *Proceedings of the IGARRS '0/12th Canadian Symposium on Remote Sensing*, Vancouver, Canada, Vol. 3, pp. 1355–1358.

Barnes, E. M., Sudduth, K. A., Hummel, J. W., Leach, S. M., Corwin, D. L., Yeng, C., Daughtry, C. S. T., and Bausch, W. C., 2003. Remote- and ground-based sensor techniques to map soil properties. *Photogrammetric Engineering & Remote Sensing*, **69**, 619–630.

Blazquez, C. H., and Edwards, G. J., 1983. Infrared color photography and spectral reflectance of tomato and potato diseases. *Journal of Applied Photographic Engineering*, **9**, 33–37.

Choudhury, B. J., 1987. Relationships between vegetation indices, radiation absorption, and net photosynthesis evaluated by a sensitivity analysis. *Remote Sensing of Environment*, **22**, 209–233.

Daughtry, C. S. T., Walthall, C. L., Kim, M. S., Brown de Colstoun, E., and McMurtrey, J. E., III, 2000. Estimating corn leaf chlorophyll content from leaf and canopy reflectance. *Remote Sensing of Environment*, **74**, 229–239.

Deering, D. W., 1978. *Rangeland Reflectance Characteristics Measured by Aircraft and Spacecraft Sensors*. PhD dissertation, College Station, TX, Texas A&M University, 338 pp.

Doraiswamy, P. C., Moulin, S., and Cook, P. W., 2003. Crop yield assessment from remote sensing. *Photogrammetric Engineering & Remote Sensing*, **69**, 665–674.

Everitt, J. H., Anderson, G. L., Esobar, D. E., Davis, M. R., Spencer, N. R., and Andrascik, R. J., 1995. Use of remote sensing for detecting and mapping leafy spurge (*Euphorbia esula*). *Weed Technology*, **9**, 599–609.

Feret, J. B., Francois, C., Asner, G. A., Gitelson, A. A., Martin, R. E., Bidel, L. P. R., Ustin, S. L., le Maire, G., and Jacquemoud, S., 2008. PROSPECT-4 and 5: advances in the leaf optical properties model separating photosynthetic pigments. *Remote Sensing of Environment*, **112**, 3030–3043.

Gates, D. M., Keegan, H. J., Schleter, J. C., and Weidner, V. R., 1965. Spectral properties of plants. *Applied Optics*, **4**, 11–20.

Gausman, H. W., and Allen, W. A., 1973. Optical parameters of leaves of 30 plant species. *Plant Physiology*, **52**(1), 57–62.

Gausman, H. W., Allen, W. A., Myers, V. I., and Cardenas, R., 1969. Reflectance and internal structure of cotton leaves *Gossypium hirsutum* L. *Agronomy Journal*, **61**, 374–376.

Gitelson, A. A., Gritz, U., and Merzlyak, M. N., 2003. Relationships between leaf chlorophyll content and spectral reflectance and algorithms for non-destructive chlorophyll assessment in higher plant leaves. *Journal of Plant Physiology*, **160**(3), 271–282.

Gitelson, A. A., Viña, A., Verma, S. B., Rundquist, D. C., Arkebauer, T. J., Keydan, G., Leavitt, B., Ciganda, V., Burba, G. G., and Suyker, A. E., 2006. Relationship between gross primary production and chlorophyll content in crops: implications for the synoptic monitoring of vegetation productivity. *Journal of Geophysical Research*, **111**, D08S11, doi:10.1029/2005JD006017.

Gitelson, A. A., Peng, Y., Masek, J. G., Rundquist, D. C., Verma, S., Suyker, A., Baker, J. M., Hatfield, J. L., and Meyers, T., 2012. Remote estimation of crop gross primary productivity with Landsat data. *Remote Sensing of Environment*, **121**, 404–412.

Haboudane, D., John, R., Millera, J. R., Tremblay, N., Zarco-Tejada, P. J., and Dextraze, L., 2002. Integrated narrow-band vegetation indices for prediction of crop chlorophyll content for application to precision agriculture. *Remote Sensing of Environment*, **81**, 416–426.

Hatfield, J. L., Asrar, G., and Kanemasu, E. T., 1984. Intercepted photosynthetically active radiation estimated by spectral reflectance. *Remote Sensing of Environment*, **14**, 65–75.

Hatfield, J. L., Prueger, J. H., and Kustas, W. P., 2004. Remote sensing of dryland crops. In Ustin, S. L. (ed.), *Remote sensing for natural resource management and environmental monitoring*, 3rd edn. Hoboken, NJ: Wiley. Manual of remote sensing, Vol. 4, Chap. 10, pp. 531–568.

Hatfield, J. L., Gitelson, A. A., Schepers, J. S., and Walthall, C. L., 2008. Application of spectral remote sensing for agronomic decisions. *Agronomy Journal*, **100**, S-117–S-131.

Huete, A. R., 1988. A soil-adjusted vegetative index (SAVI). *Remote Sensing of Environment*, **25**, 295–309.

Hunt, E. R., Everitt, J. H., Ritchie, J. C., Moran, M. S., Booth, D. T., Anderson, G. L., Clairk, P. E., and Seyfried, M. S., 2003. Applications and research using remote sensing for rangeland management. *Photogrammetric Engineering & Remote Sensing*, **69**, 675–693.

Idso, S. B., Jackson, R. D., Pinter, P. J., Jr., Reginato, R. J., and Hatfield, J. L., 1981. Normalizing the stress-degree-day parameter for environmental variability. *Agricultural Meteorology*, **24**, 45–55.

Jackson, R. D., 1983. Spectral indices in n-space. *Remote Sensing of Environment*, **13**, 409–421.

Jackson, R. D., and Huete, A. R., 1991. Interpreting vegetation indices. *Preventive Veterinary Medicine*, **11**, 185–200.

Jackson, R. D., Idso, S. B., Reginato, R. J., and Pinter, P. J., Jr., 1981. Canopy temperature as a crop water stress indicator. *Water Resources Research*, **17**, 1133–1138.

Jordan, C. F., 1969. Derivation of leaf area index from quality of light on the forest floor. *Ecology*, **50**, 663–666.

Kauth, R. J., and Thomas, G. S., 1976. The tasseled cap-A graphic description of the spectral-temporal development of agricultural crops as seen by Landsat. In *Proceedings of the Symposium on Machine Processing of Remotely Sensed Data*. West Lafayette, IN: Purdue University, pp. 41–51.

Kustas, W. P., French, A. N., Hatfield, J. L., Jackson, T. J., Moran, M. S., Rango, A., Ritchie, J. C., and Schmugge, T. J., 2003. Remote sensing research in hydrometeorology. *Photogrammetric Engineering & Remote Sensing*, **69**, 631–646.

Lass, L. W., and Callihan, R. H., 1997. The effect of phenological stage on detectability of yellow hawkweed (*Hieracium pratense*) and oxeye daisy (*Chrysanthemum leuanthemum*) with remote multispectral digital imagery. *Weed Technology*, **11**, 248–256.

Maas, S. J., 1998. Estimating cotton canopy cover from remotely sensed scene reflectance. *Agronomy Journal*, **90**, 384–388.

Markwell, J., Osterman, J. C., and Mitchell, J. L., 1995. Calibration of the Minolta SPAD-502 leaf chlorophyll meter. *Photosynthesis Research*, **46**, 467–472.

Medlin, C. R., Shaw, D. R., Gerard, P. D., and LaMastus, F. E., 2000. Using remote sensing to detect weed infestations in *Glycine max*. *Weed Science*, **48**, 393–398.

Menges, R. M., Nixon, P. R., and Richardson, A. J., 1985. Light reflectance and remote sensing of weeds in agronomic and horticultural crops. *Weed Science*, **33**, 569–581.

Moran, S., Fitzgerald, G., Rango, A., Walthall, C., Barnes, E., Bausch, W., Clarke, T., Daughtry, C., Everitt, J., Escobar, D., Hatfield, J., Havstad, K., Jackson, T., Kitchen, N., Kustas, W., McGuire, M., Pinter, P., Jr., Sudduth, K., Schepers, J., Schmugge, T., Starks, P., and Upchurch, D., 2003. Sensor development and radiometric correction for agricultural applications. *Photogrammetric Engineering & Remote Sensing*, **69**, 705–718.

Pinter, P. J., Hatfield, J. L., Schepers, J. S., Barnes, E. M., Moran, M. S., Daughtry, C. S., and Upchurch, D. R., 2003. Remote sensing for crop management. *Photogrammetric Engineering and Remote Sensing*, **69**, 647–664.

Richardson, A. J., and Weigand, C. L., 1977. Distinguishing vegetation from soil background information. *Photogrammetric Engineering and Remote Sensing*, **43**, 1541–1552.

Richardson, A. J., Menges, R. M., and Nixon, P. R., 1985. Distinguishing weed from crop plants using video remote sensing. *Photogrammetric Engineering and Remote Sensing*, **51**, 1785–1790.

Riedell, W. E., and Blackmer, T. M., 1999. Leaf reflectance spectra of cereal aphid-damaged wheat. *Crop Science*, **39**, 1835–1840.

Ritchie, J. C., Zimba, P. V., and Everitt, J. H., 2003. Remote sensing techniques to assess water quality. *Photogrammetric Engineering & Remote Sensing*, **69**, 695–704.

Rondeauz, G., Steven, M., and Baret, F., 1996. Optimization of soil-adjusted vegetation indices. *Remote Sensing of Environment*, **55**, 95–107.

Shanahan, J. F., Schepers, J. S., Francis, D. D., Varvel, G. E., Wilhelm, W. W., Tringe, J. M., Schlemmer, M. R., and Major, D. J., 2001. Use of remote-sensing imagery to estimate corn grain yield. *Agronomy Journal*, **93**, 583–589.

Tanner, C. B., 1963. Plant temperature. *Agronomy Journal*, **55**, 210–211.

Tucker, C. J., 1979. Red and photographic infrared linear combinations for monitoring vegetation. *Remote Sensing of Environment*, **8**, 127–150.

Wiegand, C. L., and Hatfield, J. L., 1988. The spectral-agronomic multisite-multicrop analyses (SAMMA) project. *International Archives of the Photogrammetry, Remote Sensing and Spatial Information Sciences*, **27**(B7), 696–706.

Wiegand, C. L., Gerbermann, A. H., Gallo, K. P., Blad, B. L., and Dusek, D., 1990. Multisite analyses of spectral-biophysical data for corn. *Remote Sensing of Environment*, **33**, 1–16.

Woolley, J. T., 1971. Reflectance and transmittance of light by leaves. *Plant Physiology*, **47**, 656–662.

Wu, C., Nu, Z., Tang, Q., and Huang, W., 2008. Estimating chlorophyll content from hyperspectral vegetative indices:

modeling and validation. *Agricultural and Forest Meteorologyis*, **148**, 1230–1241.
Zhang, V., Chen, J. M., Miller, J. R., and Noland, T. L., 2008. Leaf chlorophyll content retrieval from airborne hyperspectral remote sensing imagery. *Remote Sensing of Environment*, **112**, 3234–3247.

Cross-references

Crop Stress
Vegetation Indices

AIR POLLUTION

Annmarie Eldering
Jet Propulsion Laboratory, California Institute of Technology, Pasadena, CA, USA

Synonyms

Air quality

Definitions

Ozone. A gaseous form of oxygen with three atoms per molecule. Ozone is a bluish gas that is harmful to breathe. Nearly 90 % of the Earth's ozone is in the stratosphere and is referred to as the ozone layer. High concentrations of ozone in the lower troposphere make up one of the components of air pollution.
Troposphere. The portion of the atmosphere, which extends outward about 10–20 km from the Earth's surface and in which generally temperature decreases rapidly with altitude, clouds form, and convection and weather are active.
Stratosphere. The region of the Earth's atmosphere extending from the tropopause to about 50 km (31 miles) above the Earth's surface. The stratosphere is characterized by the presence of ozone gas (in the ozone layer) and by temperatures that rise slightly with altitude, due to the absorption of ultraviolet radiation by ozone.
Aerosols. An aerosol is a suspension of fine solid particles or liquid droplets in a gas. Some examples are pollution haze, smog, and oceanic haze.

Introduction

Air pollution refers to increased concentrations of gases or particles that are harmful to human health, vegetation, and welfare. Often, this phrase refers to gases that are regulated as air pollutants by agencies such as the Environmental Protection Agency in the United States. Specifically, the regulated pollutants are ozone, carbon monoxide, sulfur dioxide, nitrogen oxides, lead, and particulate matter. Lead is not measured by remote sensing and will not be discussed here. The study of aerosols with remote sensing is discussed in its own entry under Aerosols.

The Earth's atmosphere is described in layers, starting with the troposphere, which extends from the surface to 10–15 km, depending on location. Since humans and our biosphere occupy only the lowest layers of the atmosphere, much of the focus of studying air pollutants remains on the lowest, near-surface, layers of the troposphere. Still, there is reason to measure all layers of the troposphere, as transport of pollutants and chemical processing occurs throughout the troposphere and can impact the concentrations in the lowest layers. The stratosphere is the layer above the troposphere, and it extends from the tropopause to about 50 km above the surface. Trace gases and pollutants are distributed unequally in Earth's atmosphere, with some pollutants, like CO and SO_2, present at their highest concentrations in the troposphere. Other gases, such as ozone and NO_2, are present in both the stratosphere and the troposphere, so measuring the portion relevant to air pollution requires techniques that differentiate the troposphere and stratosphere. Remote sensing provides the capability to make measurements over a large fraction of the globe but with some limits on our ability to see the chemicals of interest in the troposphere.

This field has matured over the last 3 decades, and there are some excellent overview papers in the scientific literature that provide a history and review (Fishman et al., 2008; Martin, 2008).

This entry reviews total column measurements of CO and ozone and then discusses approaches to measure tropospheric ozone and CO. Finally, other tropospheric pollutants, namely, SO_2 and NO_2, are discussed. Note that this entry was written in 2010 and reflects the measurements up to that point in time.

Measurement of total columns of pollutants

The Measurement of Air Pollution from Satellites (MAPS) experiment was flown on the Space Shuttle four times between 1981 and 1994, and using infrared channels, it provided the first global views of CO concentrations. The technique of the Measurement of Air Pollution from Satellites (MAPS) measurement (correlation radiometer in the infrared) is most sensitive to enhancements in the mid- to upper troposphere. Measurements taken over 8–10 day periods clearly showed the high CO concentrations that came from biomass burning activities in October of 1984 and 1994, and the April 1994 measurements showed that there was some enhancement of CO across the whole Northern Hemisphere (Connors et al., 1999; Reichle et al., 1999).

A number of sensors have been used to make global measurements of CO with similar wavelengths and similar vertical sensitivity. The Japanese infrared instrument, Interferometric Monitoring of Greenhouse Gases (IMG), made global CO measurements for several months in 1996–1997 (Hadji-Lazaro et al., 1999). The Measurements of Pollution in the Troposphere (MOPITT) instrument on NASA's EOS Terra was launched in 1999 and

now has over 10 years of CO measurement data (Deeter et al., 2003). The Atmospheric Infrared Sounder (AIRS) instrument on EOS Aqua, Tropospheric Emission Spectrometer (TES) on EOS Aura, and Infrared Atmospheric Sounding Interferometer (IASI) on CNES/EUMETSAT's METOP platform have all demonstrated CO measurements from infrared channels (McMillan et al., 2005; Rinsland et al., 2006; Clerbaux et al., 2009).

In addition to CO measurements, the total column of ozone has been measured from space for decades. The Total Ozone Mapping Spectrometer (TOMS) instrument was flown in 1978, with a focus on measuring the total column ozone and contributing to our understanding of the polar ozone holes. A number of techniques have been developed to make an estimate of the amount of ozone in the stratosphere (generally from limb sounders) and take the difference of the total column ozone and the stratospheric amount to get an estimate of the tropospheric ozone. This is generally referred to as the tropospheric ozone residual (see Fishman et al., 1990) and was originally applied to TOMS total columns and SAGE stratospheric profiles. This technique has been adapted to use other column measurements (such as the Ozone Monitoring Instrument (OMI)) and other stratospheric estimates (such as MLS). While this technique provided some of the first global views of the tropospheric ozone distribution, it has limited sensitivity to the ozone in the lower troposphere.

Measurements of tropospheric ozone

An innovation in the measurement of tropospheric pollutants, especially ozone, came about with the EOS Aura Tropospheric Emission Spectrometer (TES). The TES instrument measures with very high spectral resolution (0.1 cm^{-1}) in the infrared, which allows for differentiation of tropospheric and stratospheric ozone. In cases where the surface temperatures are warm and there is a large amount of ozone, TES can differentiate the amount of ozone in the upper and lower troposphere (Worden et al., 2007; Jourdain et al., 2007). TES has provided global views of tropospheric ozone, and with the simultaneous CO measurements, the data has been used to estimate the impact of large biomass burning events on tropospheric pollution (Logan et al., 2008) and of the long-range transport of anthropogenic pollution (Zhang et al., 2006).

Ozone retrievals from infrared measurements with coarser spectral resolution (AIRS and IASI) have shown very limited sensitivity to ozone below 300 hPa (Pittman et al., 2009). A number of research algorithms have been applied to the IASI data for ozone profile retrievals, with some differences in sensitivity and biases, but they consistently show limited sensitivity below 5 km (Keim et al., 2009).

A methodology to retrieve tropospheric columns of ozone directly from satellite measurements in the ultraviolet and visible has been reported (Chance et al., 1997). This technique was demonstrated with global retrieval of tropospheric ozone column from the Global Ozone Mapping Experiment (GOME) satellite data in Liu et al., (2006). GOME (Burrows et al., 1999) was launched aboard the European Space Agency (ESA) European Remote Sensing satellite ERS-2 in 1995. This technique requires a good estimate of the tropopause height and can have limited sensitivity to lower tropospheric ozone. This technique has since been applied to the SCanning Imaging Absorption spectroMeter for Atmospheric CHartographY (SCIAMACHY) and GOME-2. SCIAMACHY (Bovensmann et al., 1999) was launched aboard ESA's Envisat in 2002, and GOME-2 (Callies et al., 2003) was launched aboard ESA's MetOp-A in 2006. Most recently, it has been applied to the NASA EOS OMI data (Liu et al., 2009).

Measurements of tropospheric CO

The MOPITT instrument was designed to exploit both thermal infrared (TIR) and near-infrared (NIR) absorption features of CO. In principal, the use of these two bands together should provide better discrimination of the tropospheric distribution of CO, providing more sensitivity to the surface than any other measurement of CO. Although MOPITT has been making measurement with both of these bands, it has been difficult to use the NIR measurements, but progress has been made on this front (Deeter et al., 2009). Recently (Worden et al., 2009), CO retrievals that combined the TIR and NIR measurements from MOPITT have been demonstrated, and they do show more sensitivity to the surface.

Other pollutants: NO_2 and SO_2

Nitrogen dioxide (NO_2) is present in the stratosphere and troposphere, but because of significant tropospheric sources and a lifetime in the troposphere that is a day or two, the variability of NO_2 is driven by tropospheric variability. This has allowed satellite measurements of NO_2 to be used to estimate the tropospheric column, by making an adjustment for the stratospheric amount, based on the column over a clean region (generally over the central area of oceans). As with ozone, this technique has been applied to many satellite measurements – GOME, SCIAMACHY, and OMI (Martin et al., 2002; Richter and Burrows, 2002; Beirle et al., 2003; Boersma et al., 2004; Bucsela et al., 2006).

Sulfur dioxide (SO_2) has been measured from a variety of UV remote sensing instruments, including TOMS (Krueger, 1983; Krueger et al., 1995), SBUV/2 (McPeters, 1993), GOME (Eisinger and Burrows, 1998), OMI (Carn et al., 2007; Yang et al., 2007; Krotkov et al., 2008), and SCIAMACHY (Lee et al., 2008). The first sulfur dioxide measurements were of volcanic eruptions, and that is the focus of most remote sensing measurements. Volcanic SO_2 is often injected into the upper troposphere and lower stratosphere in large eruptions, and this provides a strong signal in comparison to the background. Eisinger and Burrows, (1998) showed that they could measure tropospheric sulfur dioxide enhancements due to coal burning

power plants. Emissions from copper smelters and power plants have been measured with OMI (Krotkov et al., 2008), which has two orders of magnitude improvement in the minimum detectable SO_2 mass relative to TOMS, due to a smaller footprint and improvements in the wavelengths used in the retrieval.

Conclusions

A number of remote sensing techniques have been developed to detect and quantify key air pollutants in the troposphere. Using ultraviolet, visible, and infrared wavelengths, many species have now been measured over a number of years. More recently, TES on EOS Aura has demonstrated that with high spectral resolution in the infrared, stratospheric ozone can be differentiated from tropospheric ozone, and under polluted conditions, the upper and lower tropospheric ozone can be differentiated. Recent work on MOPITT data has shown that CO measurements with sensitivity near the surface can be extracted from using the 4.6 and 2.3 μm bands together.

Acknowledgment

The research to prepare this entry was carried out at the Jet Propulsion Laboratory, California Institute of Technology, under a contract with NASA.

Bibliography

Beirle, S., Platt, U., Wenig, M., and Wagner, T., 2003. Weekly cycle of NO2 by GOME measurements: a signature of anthropogenic sources. *Atmospheric Chemistry and Physics*, **3**, 2225–2232.

Boersma, K. F., Eskes, H. J., and Brinksma, E. J., 2004. Error analysis for tropospheric NO2 retrieval from space. *Journal of Geophysical Research*, **109**, D043011, doi:10.1029/2003JD003962.

Bovensmann, H., Burrows, J. P., Buchwitz, M., Frerick, J., Noel, S., Rozanov, V. V., Chance, K. V., and Goede, A. P. H., 1999. SCIAMACHY: mission objectives and measurement modes. *Journal of Atmospheric Science*, **56**, 127–150.

Bucsela, E. J., Celarier, E. A., Wenig, M. O., Gleason, J. F., Veefkind, J. P., Boersma, K. F., and Brinksma, E. J., 2006. Algorithm for NO2 vertical column retrieval from the ozone monitoring instrument. *IEEE Transactions on Geoscience and Remote Sensing*, **44**, 1245–1258.

Burrows, J. P., Weber, M., Buchwitz, M., Razonov, V., Ladstatter, A., Richter, A., De Beerk, R., Hoogen, R., Bramsdted, D., Eichmann, K. U., Eisenger, M., and Perner, D., 1999. The global ozone monitoring experiment (GOME): mission concept and first scientific results. *Journal of Atmospheric Sciences*, **56**, 151–175.

Callies, J., Corpaccioli, E., Eisinger, M., Lefebvre, A., Munro, R., Perez-Albinan, A., Ricciarelli, B., Calamai, L., Gironi, G., Veratti, R., Otter, G., Eschen, M., and van Riel, L., 2003. GOME-2 the ozone instrument on-board the European METOP satellites. *Proceedings of SPIE*, **5158**, 1–11.

Carn, S. A., Krueger, A. J., Krotkov, N. A., Yang, K., and Levelt, P. F., 2007. Sulfur dioxide emissions from Peruvian copper smelters detected by the ozone monitoring instrument. *Geophysical Research Letters*, **34**, L09801, doi:10.1029/2006GL029020.

Chance, K. V., Burrows, J. P., Perner, D., and Schneider, W., 1997. Satellite measurements of atmospheric ozone profiles, including tropospheric ozone, from ultraviolet/visible measurements in the nadir geometry: a potential method to retrieve tropospheric ozone. *Journal of Quantitative Spectroscopy and Radiative Transfer*, **51**, 461–476.

Clerbaux, C., Boynard, A., Clarisse, L., George, M., Hadji-Lazaro, J., Herbin, H., Hurtmans, D., Pommier, M., Razavi, A., Turquety, S., Wespes, C., and Coheur, P.-F., 2009. Monitoring of atmospheric composition using the thermal infrared IASI/MetOp sounder. *Atmospheric Chemistry and Physics*, **9**, 6041–6054.

Connors, V. S., Gormsen, B. B., Nolf, S., and Reichle, H. G., Jr., 1999. Spaceborne observations of the global distribution of carbon monoxide in the middle troposphere during April and October 1994. *Journal of Geophysical Research*, **104**, 21455–21470.

Deeter, M. N., Emmons, L. K., Francis, G. L., Edwards, D. P., Gille, J. C., Warner, J. X., Khattatov, B., Ziskin, D., Lamarque, J.-F., Ho, S.-P., Yudin, V., Attié, J.-L., Packman, D., Chen, J., Mao, D., and Drummond, J. R., 2003. Operational carbon monoxide retrieval algorithm and selected results for the MOPITT instrument. *Journal of Geophysical Research Atmospheres*, **108**, 4399.

Deeter, M. N., Edwards, D. P., Gille, J. C., and Drummond, J. R., 2009. CO retrievals based on MOPITT near-infrared observations. *Journal of Geophysical Research*, **114**, D04303, doi:10.1029/2008JD010872.

Eisinger, M., and Burrows, J. P., 1998. Tropospheric sulfur dioxide observed by the ERS-2 GOME instrument. *Geophysical Research Letters*, **25**, 4177–4180.

Fishman, J., Watson, C. E., Larsen, J. C., and Logan, J. A., 1990. Distribution of tropospheric ozone determined from satellite data. *Journal of Geophysical Research*, **95**, 3599–3617.

Fishman, J., et al., 2008. Remote sensing of tropospheric pollution from space. *Bulletin of the American Meteorological Society*, **89**, 805–821, doi:10.1175/2008BAMS2526.1.

Hadji-Lazaro, J., Clerbaux, C., and Thiria, S., 1999. An inversion algorithm using neural networks to retrieve atmospheric CO total columns from high-resolution nadir radiances. *Journal of Geophysical Research*, **104**, 23841–23854.

Jourdain, L., Worden, H. M., Worden, J. R., Bowman, K., Li, Q., Eldering, A., Kulawik, S. S., Osterman, G., Boersma, K. F., Fisher, B., Rinsland, C. P., Beer, R., and Gunson, M., 2007. Tropospheric vertical distribution of tropical Atlantic ozone observed by TES during the northern African biomass burning season. *Geophysical Research Letters*, **34**, L04810, doi:10.1029/2006GL028284.

Keim, C., et al., 2009. Tropospheric ozone from IASI: comparison of different inversion algorithms and validation with ozone sondes in the northern middle latitudes. *Atmospheric Chemistry and Physics (Discussion)*, **9**, 11441–11479.

Krotkov, N. A., et al., 2008. Validation of SO2 retrievals from the ozone monitoring instrument over NE China. *Journal of Geophysical Research*, **113**, D16S40, doi:10.1029/2007JD008818.

Krueger, A. J., 1983. Sighting of El Chich'on sulfur dioxide clouds with the Nimbus 7 total ozone mapping spectrometer. *Science*, **220**, 1377–1379.

Krueger, A. J., Walter, L. S., Bhartia, P. K., Schnetzler, C. C., Krotkov, N. A., Sprod, I., and Bluth, G. J. S., 1995. Volcanic sulfur dioxide measurements from the total ozone mapping spectrometer instruments. *Journal of Geophysical Research*, **D100**, 14057–14076.

Lee, C., Richter, A., Weber, M., and Burrows, J. P., 2008. SO2 retrieval from SCIAMACHY using the weighting function DOAS (WFDOAS) technique: comparison with standard DOAS retrieval. *Atmospheric Chemistry and Physics*, **8**, 6137–6145.

Liu, X., et al., 2006. First directly retrieved global distribution of tropospheric column ozone from GOME: comparison with the GEOS-CHEM model. *Journal of Geophysical Research*, **111**, D02308, doi:10.1029/2005JD006564.

Liu, X., Bartia, P. K., Chance, K., Spurr, R. J. D., and Kurosu, T. P., 2010. Abstract ozone profile retrievals from the ozone

monitoring instrument. *Atmospheric Chemistry and Physics Discussions*, **9**, 22693–22738.
Logan, J. A., Megretskaia, I., Nassar, R., Murray, L. T., Zhang, L., Bowman, K. W., Worden, H. M., and Luo, M., 2008. Effects of the 2006 El Niño on tropospheric composition as revealed by data from the tropospheric emission spectrometer (TES). *Geophysical Research Letters*, **35**, L03816, doi:10.1029/2007GL031698.
Martin, R. V., 2008. Satellite remote sensing of surface air quality. *Atmospheric Environment*, **42**, 7823–7843.
Martin, R.V., and Coauthors, 2002. An improved retrieval of tropospheric nitrogen dioxide from GOME. *Journal of Geophysical Research*, **107**, 4437, doi:10.1029/2001JD001027
McMillan, W. W., Barnet, C., Strow, L., Chahine, M. T., McCourt, M. L., Warner, J. X., Novelli, P. C., Korontzi, S., Maddy, E. S., and Datta, S., 2005. Daily global maps of carbon monoxide from NASA's atmospheric infrared sounder. *Geophysical Research Letters*, **32**, L11801, doi:10.1029/2004GL021821.
McPeters, R. D., 1993. The atmospheric SO2 budget for Pinatubo de-rived from NOAA-11 SBUV/2 spectral data. *Geophysical Research Letters*, **20**, 1971–1974.
Pittman, J. V., Pan, L. L., Wei, J. C., Irion, F. W., Liu, X., Maddy, E. S., Barnet, C. D., Chance, K., and Gao, R.-S., 2009. Evaluation of AIRS, IASI, and OMI ozone profile retrievals in the extratropical tropopause region using in situ aircraft measurements. *Journal of Geophysical Research*, **114**, D24109, doi:10.1029/2009JD012493.
Reichle, H. G., et al., 1999. Space shuttle based global CO measurements during April and October 1994, MAPS instrument, data reduction, and data validation. *Journal of Geophysical Research*, **104**, 21443–21454.
Richter, A., and Burrows, J. P., 2002. Tropospheric NO2 from GOME measurements. *Advances in Space Research*, **29**, 1673–1683.
Rinsland, C. P., Luo, M., Logan, J. A., Beer, R., Worden, H. M., Worden, J. R., Bowman, K., Kulawik, S. S., Rider, D., Osterman, G., Gunson, M., Goldman, A., Shephard, M., Clough, S. A., Rodgers, C., Lampel, M., and Chiou, L., 2006. Nadir Measurements of carbon monoxide distributions by the tropospheric emission spectrometer onboard the Aura spacecraft: overview of analysis approach and examples of initial results. *Geophysical Research Letters*, **33**, L22806, doi:10.1029/2006GL027000.
Worden, H. M., Logan, J., Worden, J. R., Beer, R., Bowman, K., Clough, S. A., Eldering, A., Fisher, B., Gunson, M. R., Herman, R. L., Kulawik, S. S., Lampel, M. C., Luo, M., Megretskaia, I. A., Osterman, G. B., and Shephard, M. W., 2007. Comparisons of tropospheric emission spectrometer (TES) ozone profiles to ozonesodes: methods and initial results. *Journal of Geophysical Research*, **112**, D03309, doi:10.1029/2006JD007258.
Worden, H. M., Deeter, M. N., Edwards, D. P., Gille, J. C., 2009. Multispectral retrieval of CO from MOPITT. *Eos Transactions, AGU*, 90, Fall meeting supplement, Abstract U33B–0059.
Yang, K., Krotkov, N. A., Krueger, A. J., Carn, S. A., Bhartia, P. K., and Levelt, P. F., 2007. Retrieval of large volcanic SO2 columns from the Aura ozone monitoring instrument: comparison and limitations. *Journal of Geophysical Research*, **112**, D24S43, doi:10.1029/2007JD008825.
Zhang, L., et al., 2006. Ozone-CO correlations determined by the TES satellite instrument in continental outflow regions. *Geophysical Research Letters*, **33**, L18804, doi:10.1029/2006GL026399.

Cross-references

Optical/Infrared, Atmospheric Absorption/Transmission, and Media Spectral Properties
Stratospheric Ozone
Trace Gases, Troposphere - Detection from Space

ATMOSPHERIC GENERAL CIRCULATION MODELS

Joao Teixeira[1], Mark Taylor[2], Anders Persson[3] and Georgios Matheou[1]
[1]Jet Propulsion Laboratory, California Institute of Technology, Pasadena, CA, USA
[2]Sandia National Laboratory, Albuquerque, New Mexico, USA
[3]United Kingdom Meteorological Office, Exeter, Devon, UK

Definition

Atmospheric general circulation models (atmospheric GCMs) are mathematical models based on numerically discretized versions of differential equations that describe the atmospheric physics and dynamics, which are utilized to simulate the global atmospheric circulation. Atmospheric GCMs have several practical applications including medium-range (typically 3–10 days) weather forecasting, (see entry *Weather Prediction*), seasonal forecasting (typically 3–12 months) when coupled to models of other components of the climate system such as the global ocean, and climate prediction (typically 10–1,000 years) when models of the various components of the climate system, such as sea and land ice, carbon-cycle, and biosphere models, are incorporated.

Introduction and short history

Atmospheric general circulation models are based on the fundamental fluid dynamics and thermodynamics equations that govern the transport of momentum, energy, water mass, and chemical species in the atmosphere. The essential fluid dynamics and thermodynamics equations were formalized during the nineteenth century leading to the Navier–Stokes equations, the energy conservation equation, and the introduction of the Coriolis effect in the momentum conservation equations.

When meteorological weather forecast services were established around the world in the second half of the nineteenth century, their practitioners were often compared with their astronomical colleagues, who could accurately predict celestial events such as eclipses and the return of comets. However, weather forecasters, relying on empirical rules and experience, often had difficulties in accurately predicting next day's weather.

In the early twentieth century, Vilhelm Bjerknes (1904), proposed that weather prediction should be based on the fundamental equations of fluid dynamics and energy conservation. Accordingly, weather could, in principle, be predicted along the same lines as the motions of celestial bodies.

In 1922, L. F. Richardson (Richardson, 1922) publishes a groundbreaking book on numerical weather prediction where he basically sets up the agenda for the entire field and describes in detail an example of a forecast. However, and besides the fact that his forecast appeared as fairly inaccurate, it was quite clear that the amount of required

numerical computations, if done by humans, was impossibly large in operational terms so as to be able to produce forecasts much faster than the real weather. In order to overcome this problem, Richardson envisioned a future where thousands of "human calculators" would be working together in a single room producing weather forecasts for the whole world.

The situation changed dramatically with the advent of computers after World War II, when John von Neumann thought of weather prediction as one of the most obvious applications of the new tremendous numerical power provided by computers – in fact, von Neumann was not as interested in weather forecasting per se, as he was interested in computational models of the atmospheric general circulation. During this period, a substantial amount of research was carried out in creating the field of numerical analysis of differential equations. In the mid-1950s, Norman A. Phillips developed the first general circulation model of the global atmosphere (e.g., Randall, 2000).

Model dynamics

Modern global weather and climate prediction models are made up of several component models (i.e., atmosphere, land, ocean, ice). The models of the atmospheric component, or atmospheric GCMs, have two main building blocks: (1) model dynamics, representing the large-scale motions of the Earth's atmosphere, and (2) model physics, which includes a suite of parameterizations of sub-grid-scale physical processes (see below). It is the dynamical core's role to solve the partial differential equations that describe the large-scale motions. The heating, cooling, and mixing processes represented by the model physics appear as forcing terms in these equations. Errors in both the model physics and dynamics can have significant impacts in terms of weather and climate predictability.

Atmospheric dynamics are well approximated by numerical solutions of the Navier–Stokes equations, but as in almost all fluid dynamics applications, this approach is far too computationally expensive because of the large spectrum of scales present in global weather and climate prediction problems. Atmospheric GCMs use modified equations, which still capture important features of atmospheric dynamics, such as cyclones, anticyclones, frontal zones, and jet streams while neglecting inconsequential processes for weather and climate forecasting such as acoustic waves (see entry *Acoustic Waves, Propagation*). A common choice are the atmospheric *primitive equations*, which also neglect small terms related to spherical geometry, small terms related to the Coriolis effect, and some small vertical acceleration terms (the hydrostatic approximation).

The computational domain of a GCM is the thin spherical shell containing the Earth's atmosphere. One of the defining characteristics of a dynamical core is how it handles this spherical domain. The grids used in GCMs are constructed by decomposing a three-dimensional grid into a two-dimensional grid for conforming to the surface of the sphere (the *horizontal grid*) and a one-dimensional grid in the radial direction (the *vertical grid*). For the horizontal grid, there are three main approaches all of which have strengths and weaknesses.

One approach is to use a mesh of equally spaced points in latitude and longitude. These grids are highly structured but have a severe clustering of grid points at both poles, creating some numerical challenges collectively referred to as the pole problem. There are many effective numerical treatments of the pole problem, one of the most successful being the spherical harmonic expansions used by global spectral methods, but they often degrade parallel scalability (the ability to efficiently use multiprocessor computers in order to speed up the numerical solution of the equations).

A second approach is to decompose the sphere into several regions, each of which is meshed with a quasi-uniform grid without poles. The resulting grids must be stitched together, using a composite or overset grid method. This stitching process can make it difficult to numerically conserve mass and energy in a physically consistent way.

The third approach is to use an arbitrary tiling of the surface of the sphere with polygons, usually spherical triangles, quadrilaterals, or a combination of hexagons and pentagons. These grids are challenging for finite difference methods and are most effectively utilized by finite element and finite volume methods designed for fully unstructured grids. The choice depends on the application needs in terms of accuracy, numerical conservation properties, and parallel scalability.

Model physics

The problem of physical parameterization in fluids is as old as the first modern studies of turbulence in the nineteenth century. It was apparently clear from the start, at least to some, that for turbulent fluids, such as the atmosphere, it is not feasible or even relevant to try to follow every parcel of fluid in its turbulent trajectory. Instead, it was suggested from the early twentieth century that research should concentrate on trying to understand the statistical properties of turbulent flows.

The numerical discretizations in weather and climate prediction models imply a limit for the temporal and spatial scales below which the fluid motions cannot be resolved by the model. Because of the nonlinear nature of the atmosphere, the unresolved small scales can have a fundamental influence over the resolved large scales. Since there is no way of explicitly knowing in detail what happens at the sub-grid scales, the physics at these scales has to be parameterized as a function of the resolved motions. What can be estimated about the model variables at scales smaller than the horizontal grid scale are their statistical properties such as joint probability density functions (PDF) within the grid box. Ultimately, for

turbulence and convection, the essential problem of parameterization is how to estimate these PDFs at every model grid point.

It is natural to divide atmospheric physics parameterizations into two main groups: (1) the parameterization of radiation and cloud microphysics and (2) the parameterization of convective and turbulent mixing and associated cloud structure. Radiation and cloud microphysics parameterizations represent physical interactions that occur at extremely small scales from the atomic and molecular scales to cloud droplet scales. Turbulence and convection parameterizations, as discussed before, attempt to represent in a large-scale, atmospheric flow that occurs at scales smaller than the typical grid size (on the order of 10–100 km in the horizontal) of atmospheric GCMs. As such, they do represent fundamentally different physics and are often treated using different mathematical and conceptual tools.

Overall, in modern atmospheric GCMs, there are several different physical processes that need to be parameterized, which are traditionally classified as *follows*: turbulence or boundary layer parameterizations that represent sub-grid vertical motions within the boundary layer (i.e., the region of the atmosphere where turbulence is most prevalent, from the surface to about 1 km height); moist convection parameterizations that represent sub-grid vertical flow due to convective motions driven by condensation/evaporation processes associated with convective towers; cloud parameterizations that represent sub-grid clouds and condensation/evaporation processes, including cloud microphysics; longwave and shortwave radiation; interactions with the ocean and land surface; and sub-grid orographic effects (e.g., gravity wave drag). More detailed information regarding atmospheric general circulation models in general, and model physics and dynamics in particular, can be found in Haltiner and Williams (1983), Randall (2000), and Washington and Parkinson (2005).

Acknowledgment

This research was carried out at the Jet Propulsion Laboratory, California Institute of Technology, under a contract with the NASA.

Bibliography

Bjerknes, V., 1904. Das problem der wettervorhersage, betrachtet vom stanpunkt der mechanic und der physic. *Meteorologische Zeitschrift*, **21**, 1–7.

Haltiner, G. J., and Williams, R. T., 1983. *Numerical Prediction and Dynamic Meteorology*, 2nd edn. New York: Wiley, p. 477.

Randall, D. A., 2000. *General Circulation Model Development: Past, Present, and Future*. London: Academic, Vol. 70, p. 416.

Richardson, L. F., 1922. *Weather Prediction by Numerical Processes*. London: Cambridge University Press, p. 236.

Washington, W., and Parkinson, C. L., 2005. *An Introduction to Three-Dimensional Climate Modeling*, 2nd edn. Sausalito: University Science, p. 354.